THE UNIVERSITY OF CHICAGO

TOPOLOGICAL GYROSCOPIC METAMATERIALS

A DISSERTATION SUBMITTED TO
THE FACULTY OF THE DIVISION OF THE PHYSICAL SCIENCES
IN CANDIDACY FOR THE DEGREE OF
DOCTOR OF PHILOSOPHY

DEPARTMENT OF PHYSICS

BY
LISA MICHELLE NASH

CHICAGO, ILLINOIS
AUGUST 2017

To my family

TABLE OF CONTENTS

LIST OF FIGURES

ACKNOWLEDGMENTS

Finishing a PhD feels like a monumental task. Though I have worked hard to get here, I know that it would not have been possible without many supporters. I have spent five years at UChicago, but graduating from this PhD program is the result of many more years of work by more individuals than just myself. Here I'd like to reflect on those who have helped me personally as well as professionally.

First and foremost, I'd like to acknowledge my mom, dad, and mamaw. Without their early commitment to my education and development, I would never have been able to finish (or even enter) this PhD program. Beyond academics, they helped form my values and shape me into the person I am today.

I'd also like to acknowledge my twin sister, Jessica Nash. We have gone through many of life's obstacles together. In grad school, we even got to have our first papers published in the same month, and are now defending less than two months apart! Our daily conversations helped me navigate the stresses of grad school. Thank you for always being my friend.

My research adviser from UNC, Hugon Karwowski ("Dr. K"), was instrumental in bringing me here today. During my physics career, Dr. K mentored me through research, class selection, REUs, and grad school applications. Even during my PhD, he answered emails and had occasional phone calls with me to check in and give advice.

Of course, I also have to thank my colleagues and friends in the Irvine group. Though I won't name everyone here, I enjoyed working with all of you. I'd like to thank Vishal Soni for always making me laugh, Martin Scheeler for helping my conquer my fear of improv, Noah Mitchell for being a good friend and great to work with on the gyro project, Hridesh Kedia for always listening, and Sofia Magkiriadou and Stephane Perrard for being willing to give input on my work and being optimistic officemates.

It has been a lot of fun to work on this project, so I'd also like to thank my collaborators and coauthors. In particular, this work would not have been possible without the ideas of Ari Turner, William Irvine, and Vincenzo Vitelli. The project would not have turned out the

same without the input and work of Noah Mitchell, Alismari Read, and Dustin Kleckner.

Finally, I thank my adviser, William, for providing the opportunity to work on such an interesting and unique project in my time at UChicago. I learned a lot about presenting my work in an engaging way, and communication in general. I hope to carry forward lessons I learned into my future career.

ABSTRACT

Topological materials are generally insulating in their bulk, with protected conducting states on their boundaries that are robust against disorder and perturbation of material properties. The existence of these conducting edge states is characterized by an integer topological invariant. Though the phenomenon was first discovered in electronic systems, recent years have shown that topological states also exist in classical systems.

In this work we explore the topological properties of gyroscopic materials, which are created by coupling networks of fast-spinning objects. Through a series of simulations, numerical calculations, and experiments, we show that these materials can support topological edge states. We find that edge states in these gyroscopic metamaterials bear the hallmarks of topology related to broken time reversal symmetry: they transmit excitations unidirectionally that are extremely robust against experimental disorder and can be characterized with a Chern number. We also study requirements for topology by studying several lattice configurations and find that a simple prescription can be used to create many gyroscopic lattices. Though many of our gyroscopic networks are periodic, we explore amorphous point-sets and find that topology also emerges in these systems without long-range order.

CHAPTER 1

INTRODUCTION

1.1 Topology in Quantum and Classical Systems

Condensed matter physics has traditionally dealt with the discovery and classification of materials into distinct phases. For example, material band-structure determines electrical conductivity and classification of an electronic material as either an insulator or a conductor. In the early 1980s, an additional "topological" phase was uncovered with the discovery of the Quantum Hall Effect (QHE). Since then, the revelation that the band structures of electronic insulators may be topologically non-trivial has sparked an explosion of research into "topological" phases of electronic matter [1, 2, 3].

Though there are many examples of topological materials, generally speaking they share common qualities: they are insulating in their bulk and have protected conducting states on their boundaries or surfaces. They are also classified by an integer "topological invariant" that is usually calculated using the material's momentum-space eigenstates.

The QHE exhibits the robust conducting edge states that are commonly recognized as hallmarks of topology today, but additionally includes the property of quantized Hall conductance which is related to its topological invariant. Because of the quantized nature of early topological materials, the phenomenon was first thought to be unique to quantum mechanics. However, examination of the underlying mathematics and later research has shown that classical systems can also support nontrivial band topology and robust edge states. The first examples of classical topological systems were photonic and were theoretically proposed by Raghu and Haldane in 2008 [4].

Recent years have seen many more examples of classical systems with nontrivial band topology including examples in mechanics. Topology in mechanical systems was first theoretically proposed by Prodan in 2009 [5], and it was in 2013 with the influential work of Kane and Lubensky that topological acoustic and mechanical materials began to be a major av-

enue of research in condensed matter physics. Kane and Lubensky established a connection between mechanical modes and topological band theory of electronic systems. They found that in the linear regime, zero-frequency modes in certain isostatic lattices were bound to material edges and topologically protected [6].

Interestingly, further analysis of these topological mechanical materials have shown some behavior that is not shared with their electronic counterparts. Namely, propagating solitons have been theoretically proposed and experimentally observed [7].

Since then, topological states have also been uncovered in mechanical systems at finite frequency in rotating fluids, coupled pendula, and as in the case of this thesis, in networks of coupled gyroscopes. Both zero and finite frequency topological materials may have quite useful properties in many instances: they promise better control of material failure, or as in the case of this work, guided vibration transmission.

At first glance, it may seem that mechanical and quantum systems are fundamentally different because the nature of the equations that govern them are dissimilar in order of the time derivative. There are various methods for dealing with this difference. This thesis shows an example where classical equations can be mapped to directly to the an electronic tight-binding model and then analyzed using that framework. Similar methods are often used in mechanical systems and it has been found that like their electronic counterparts, topological mechanical systems can then be classified based on symmetries [8].

We focus our attention on a system that breaks time reversal symmetry and whose topology is therefore studied via a Chern number [3]. The Chern number is calculated as a bulk quantity, but relates to the number of edge states through the bulk-boundary correspondence, equation 1.1:

$$N_R - N_L = \Delta C. \tag{1.1}$$

For a particular gap, the bulk-boundary correspondence relates the number of right-moving (N_R) and left-moving (N_L) edge modes to the difference in Chern number in the band-gap

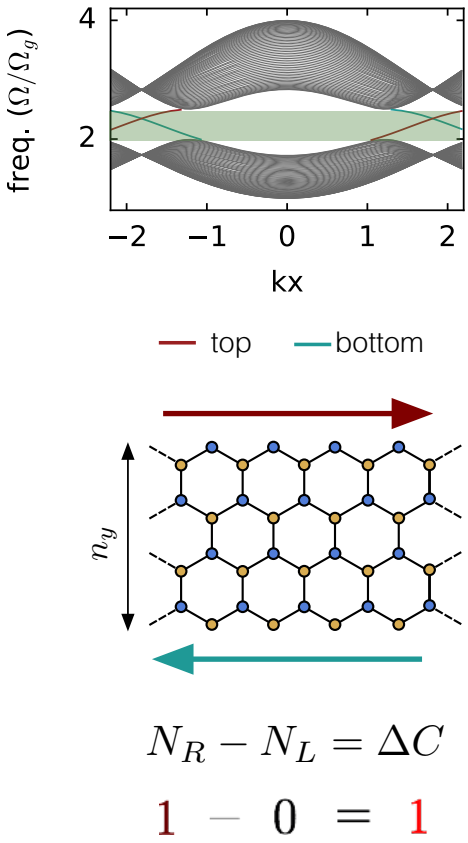

Figure 1.1: *Illustration of bulk-boundary correspondence.* The Chern number is related to the edge states of a material via the bulk-boundary correspondence. This figure shows the band-structure for a gyroscope strip that is infinite in the x direction. A band-gap is labeled in green. This band-structure shows states with a positive group velocity on the top of the strip and states with a negative group velocity on the bottom of the strip. The Chern number is 1.

(ΔC) across the boundary [3], as illustrated in Fig. 1.1.

A Chern number is defined for each band in a materials' band structure and must sum to zero across all bands. In electronic systems, the sum of the Chern number of bands beneath the Fermi level determines the material topology. In our mechanical system, we find the sum of the bands beneath each gap.

Chern numbers which are non-zero imply the existence of a "non-trivial" band topology and the existence of chiral edge states. This thesis will demonstrate that coupled gyroscopic systems can be topologically non-trivial and explores the further requirements for topology.

1.2 Thesis overview

We begin in Chapter 2 by examining the equations of motion that govern gyroscopic materials. We show that the geometry of gyroscopic lattices is an integral component in the determination of symmetries in gyroscopic systems, and discuss characterization of these materials' band-structures with a Chern number. We additionally show that our gyroscopic materials can be mapped to the electronic Haldane model [2], when the coupling between gyroscopes is low in comparison to the force our gyroscopes feel from gravity.

In Chapter 3, we discuss the first theoretical exploration and experimental observation of topology in gyroscopic metamaterials on a honeycomb lattice. We show that a numerical model can accurately predict experimental edge states–even with a significant amount of disorder. We demonstrate that time reversal symmetry is entirely dependent on lattice geometry, and show how edge state direction can be controlled by manipulating lattice geometry.

Chapter 4 extends our work to other lattice configurations and explores requirements for achieving topology in gyroscopic systems. We examine topological dependence on the competition between time reversal, inversion symmetries, and other lattice properties such as connectivity and coordination number. We develop a simple procedure that can be used to generate topological gyroscopic lattices.

We show that the topological phase of gyroscopic materials can be manipulated in experiment in Chapter 5. These experiments pave the way for tunable topological gyroscopic materials. In Chapter 6, we additionally show that even networks without underlying spatial order are able to support topological edge states.

CHAPTER 2

EQUATIONS FOR LATTICE GYROSCOPIC MATERIALS

2.1 Introduction

In topological mechanical systems, as in electronic systems, symmetries play an important role in determining material properties [8]. This thesis focuses on a system with broken time reversal symmetry, which has been found to be an integral component in the description and classification of electronic materials. Throughout this thesis, the same governing equations are used to study each gyroscopic material. Here, we will provide an introduction and explain insights from study of these equations.

Gyroscopic metamaterials combine physics from traditional mechanics and electronic systems because lattice vibrations in these systems can be mapped directly to electrons in a hopping model. However, these materials differ from electronic tight binding models in a significant way. In electronic tight binding models, a magnetic field must be applied in order to break time reversal symmetry. In contrast, time reversal symmetry in gyroscopic systems is entirely dependent on the lattice geometry. As we will show, it is impossible to change whether time reversal symmetry is broken without deforming an underlying lattice. Interestingly, this implies that the existence of topological modes is dependent on lattice geometry.

In order to understand the unique properties of gyroscopic metamaterials, we study the effects of time reversal symmetry on the linearized equation of motion in real space. We then move on to the method of characterizing topology via band-structure and Chern number calculation. Finally, we discuss the direct mapping of gyroscopic systems to the topological Haldane model.

2.2 The linearized equation of motion and time reversal symmetry

Here we discuss how the connection between time reversal symmetry and lattice geometry can be ascertained from the linearized equation of motion and discuss the calculation of the Chern number of these networks.

Our metamaterial is composed of gyroscopes which hang from a pivot point and spin rapidly enough for their angular momentum to lie approximately along the primary axis. as shown in Figure 2.1(A). This thesis studies gyroscopes in the "fast-spinning limit", where only gyroscopic precession must be considered. In this case, the free tip of a gyroscope moves when a torque acts about the pivot point according to:

$$\vec{\tau} = \vec{\ell_f} \times \vec{F} \tag{2.1}$$

where $\vec{\ell_f}$ as the vector from the pivot point to the point acted upon by force, $\vec{F}$, as denoted in Fig. 2.1(A).

Considering small displacements of the gyroscope tip allows a linearized description of our system. In this case, the displacement approximately lies in the plane containing the gyroscope tips. Denoting the displacement from the equilibrium position in the plane as $\psi = \delta x + i\delta y$, the cross product in Eqn. 2.1 is performed by multiplying by an imaginary coefficient. The equation of motion for a single gyroscope under the influence of gravity can then be derived:

$$\dot{\psi} = i\frac{mg\ell_{mg}}{I\omega}\psi. \tag{2.2}$$

The motion of the object described in Eqn. 2.2 is fundamentally different from the motion of a swinging pendulum. The response of the object is perpendicular to the force that is applied – causing the gyroscope tip to move in a circle in a constant gravitational field rather

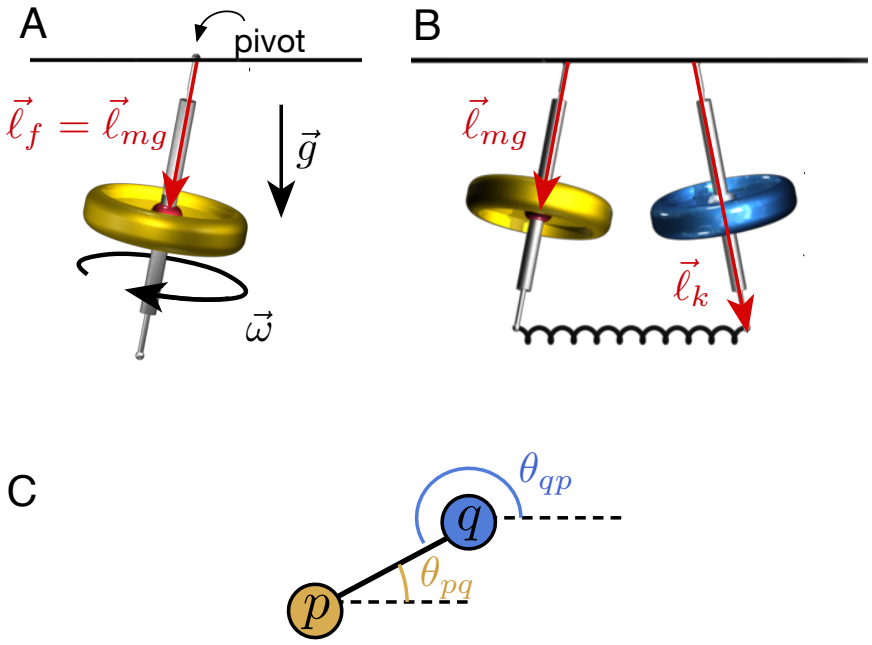

Figure 2.1: *A spring-coupled gyroscopic metamaterial. (A)* Gyroscopes spinning with angular velocity $\vec{\omega}$ which hanging from a pinned pivot point. $\vec{\ell_f}$ is the vector from the pivot point to where a force acts. When the only force is gravity, $\vec{\ell_f} = ell\vec{_{mg}}$ *(B)* Gyroscopes in the metamaterial are coupled to their neighbors in the lattice via a spring which is attached to the free end. *(C)* The linearized equation of motion for our system relates the displacements via angles between bonds and the local gyroscope's local x-axis (indicated by dotted lines in this view from above).

than just swinging back and forth.

Eqn. 2.2 bears resemblance to the Schrödinger equation in that it is first-order in time and has an imaginary coefficient. In accordance with this resemblance, we study time reversal symmetry using the same set of operations as in quantum mechanics: $\psi \to \psi^*$ and $t \to -t$. The operation $\psi \to \psi^*$ carries out a reflection of the gyroscope's displacement about an axis in the plane of the gyroscope tips, as shown in, instead of reversing the gyroscope's momentum, which is the usual time reversal operation. Due to the geometric component to the time-reversal operation, lattice geometry plays an important role in gyroscopic networks – as will be discussed further later in this work. The time-reversal operation as described above conserves the equation of motion Eqn. 2.2, indicating that gravitational interactions alone are not enough to break time reversal symmetry in gyroscopic systems.

Interacting gyroscopes, however, possess the potential to break time reversal symmetry. Each gyroscope's displacement from equilibrium, ψ, can be expressed in terms of a local coordinate system with origin at its equilibrium position. A choice of local $x-$axis for two coupled gyroscopes is depicted in by dotted lines Fig. 2.1C.

For linear springs, we need only to consider displacements which are along the bond. For gyroscopes p and q, it is convenient to extract the component of $\psi_p - \psi_q$ along the bond by rotating the system to the local $x-$axis of p, taking the real part of expression, and then rotating back, Fig. 2.2. The resulting force in complex form is given by:

$$F_{pq} = -k_0 e^{i\theta_{pq}} \mathrm{Re}[e^{-i\theta_{pq}}(\psi_p - \psi_q)] \tag{2.3}$$

$$= -\frac{k_0 e^{i\theta_{pq}}}{2}\left[e^{-i\theta_{pq}}(\psi_p - \psi_q) + e^{i\theta_{pq}}(\psi_p^* - \psi_q^*)\right], \tag{2.4}$$

where k_0 is the spring constant of the bond. Using this result, the equation of motion for

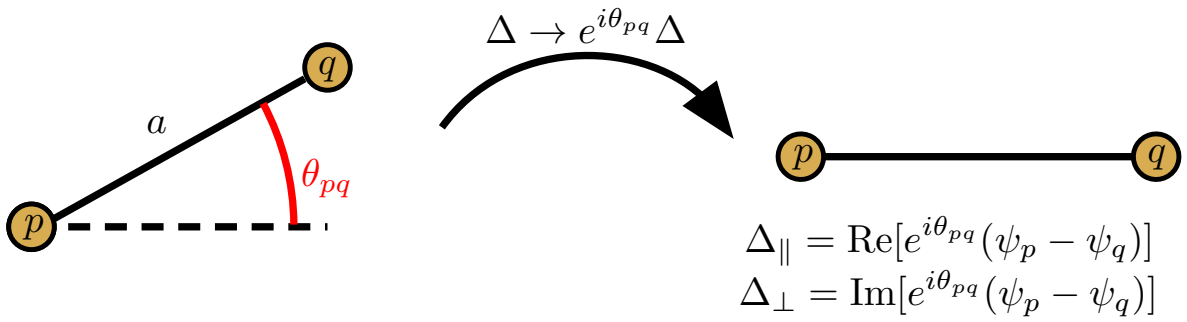

Figure 2.2: *Derivation of the linearized gyroscopic equation of motion.* The linearized equation of motion for two interacting gyroscopes can be derived by imagining rotating the bond to the x-axis.

two gyroscopes can then be written as:

$$ie^{i\theta_{pq}}\dot{\psi}_p e^{-i\theta_{pq}} = -\left(\frac{\Omega_k e^{i\theta_{pq}}}{2}\left[e^{-i\theta_{pq}}\left(\psi_p - \psi_q\right) + e^{i\theta_{pq}}\left(\psi_p^* - \psi_q^*\right)\right] + \Omega_{gp}\psi_p\right). \tag{2.5}$$

where $\Omega_k = k_0\ell_e^2/(I\omega)$ and $\Omega_{gp} = mg\ell_{mg}/(I\omega)$. Eqn. 2.5 shows clearly that time reversal symmetry is related to geometry: When reflections are perpendicular or parallel to the bond-in-question, time reversal symmetry is conserved. Time reversal symmetry is protected under these operations because energy is conserved in both the case when reflections are parallel and perpendicular to the connecting bond. This can be shown by considering the energy change which occurs due to the time-reversal operation. The stretching/compression, Δ_{sc}, of the spring is given by: $\Delta_{sc} \propto (r_{x1} - r_{x2})\cos\theta_{12} + \left(r_{y1} - r_{y2}\right)\sin\theta_{12}$. When the gyroscopes' displacement is mirrored in the y-axis ($\psi \to \psi^*$ or $r_y \to -r_y$), in general the spring length will be unchanged only if $\sin\theta_{12} = 0$, i.e. if the mirror axis aligns with the equilibrium bond

angle. However, if $\cos\theta_{12} = 0$, or the mirroring axis is perpendicular to the bond, then the spring energy, $E_k \propto \Delta^2$, is conserved by converting stretching to compression, as discussed in section 3.2.

The full equation of motion for a hanging gyroscope with more than one neighbor is a sum over the neighboring gyroscopes, q, and can be similarly expressed:

$$i\frac{d\psi_p}{dt} = -\Bigg(\frac{\Omega_k}{2}\sum_q^{n.n.}\Big[\left(\psi_p - \psi_q\right) + e^{2i\theta_{pq}}\left(\psi_p^* - \psi_q^*\right)\Big] + \Omega_{gp}\psi_p\Bigg). \tag{2.6}$$

As before, time reversal symmetry is preserved if all reflections are parallel or perpendicular to bond axes, or equivalently, if a coordinate system can be chosen such that the prefactor $e^{2i\theta_{pq}}$ is real for all bonds in the network.

2.3 Band structure and Chern number calculations on a lattice

We have shown that we can study the lattice geometry to determine whether time reversal symmetry is broken. However, the question of topology requires calculation of a Chern number, which is the integral of the Berry curvature over the Brillouin zone. To calculate the Chern number for gyroscopes on a lattice, we find the band-structure using the linearized equation of motion, Eqn. 2.6. For each site in a unit cell, we assume a solution which is composed of clockwise and counter-clockwise propagating modes:

$$\psi_A = \psi_{A,R}e^{i(\vec{k}\cdot\vec{x}-\omega t)} + \bar{\psi}_{A,L}e^{-i(\vec{k}\cdot\vec{x}-\omega t)}, \tag{2.7}$$

where A indexes the n sites in a unit cell. The resulting equations can be expressed as the $2n \times 2n$ dynamical matrix which is a function of the wave vector, $\vec{k}$. This dynamical matrix resembles hopping model matrices seen for lattice calculations in quantum mechanics.

Diagonalizing the dynamical matrix yields $2n$ frequencies of the dispersion bands at each

value of $\vec{k}$. The eigenvalues come in positive/negative pairs, but each pair represents the same oscillation in real space. Because of this redundancy, we discuss only the positive eigenvalues for each system. At each value of $\vec{k}$, each mode has a corresponding eigenvector, $\left|u_j(\vec{k})\right\rangle$, characterizing the amplitudes and phases of the gyroscopes' collective motion.

The Chern number of each band is given by an integral of the Berry curvature $\mathcal{F}(\vec{k})$:

$$\begin{aligned} C_j &= \frac{1}{2\pi}\int d^2k\ \mathcal{F}_j(\vec{k}) \\ &= \frac{i}{2\pi}\oint A_j(k)\cdot dk, \end{aligned} \tag{2.8}$$

where $A_j(k) = i\langle u_j|\nabla_k u_j\rangle$. In this work, Chern numbers are calculated numerically using the phase-invariant formula [9]

$$C_j dx\wedge dy = \frac{i}{2\pi}\int d^2k\ \mathrm{Tr}[dP_j\wedge P_j dP_j], \tag{2.9}$$

where $P_j \equiv |u_j\rangle\langle u_j|$ is the projection matrix and $\wedge$ is the wedge product.

2.4 Mapping to the topological Haldane model

Haldane's model has been widely used since its conception as a conceptual basis for theoretical and experimental research exploring topology in many systems [10]. Here we show that in the limit of weak interactions, that gyroscopic metamaterials map to the Haldane model.

We can reduce the complexity of finding the lattice band structure and map our system to a tight-binding calculation by considering the case where $\Omega_g \gg \Omega_k$. Although most calculations presented in this thesis are not in this regime, it is still useful for studying the topology of band structures. We may study the system in this regime because the topology of a band gap can only change when the gap closes and reopens. Therefore, we may analyze systems in the Haldane model limit as long as the band gap does not close with decreasing values of Ω_k/Ω_g.

To ensure that the gap stays open with variation of this ratio, we study the relationship between between Ω_k, Ω_g and the gap width, W, in the honeycomb lattice. This can be solved for analytically as shown in Eqn. 2.10:

$$\frac{W}{\Omega_g} = \left(\frac{3}{2}R + 1 - \sqrt{3R+1}\right), \tag{2.10}$$

where R is the ratio Ω_k/Ω_g. In the limit of strong pinning ($\Omega_g \gg \Omega_k$), $W \approx (9/8)\Omega_k^2/\Omega_g$. For other lattices, we expect that the gap width will scale similarly, though the details on the right hand side of Eqn. 2.10 will change with changing lattice geometries.

When $\Omega_g \gg \Omega_k$, the motion of each gyroscope is approximately circular and we may write the displacement of the gyroscope as $\psi_n = e^{-i\Omega t}u_n + e^{i\Omega t}v_n^*$, where u_n is the amplitude of precession determined by gravity and v_n is the counter-rotating amplitude, and Ω is the precession frequency of the normal mode. With the displacement written in this way, our equation of motion can be written as shown in Eqn. 2.11 and Eqn. 2.12 for clockwise and counterclockwise precessing modes:

$$\Omega u_n = \Omega_g u_n + \frac{1}{2}\Omega_k \sum_m (u_n - u_m) + \frac{1}{2}\Omega_k \sum_m (v_n - v_m)e^{2i\theta_{nm}}, \tag{2.11}$$

$$-\Omega v_n = \Omega_g v_n + \frac{1}{2}\Omega_k \sum_m (v_n - v_m) + \frac{1}{2}\Omega_k \sum_m (u_n - u_m)e^{-2i\theta_{nm}}. \tag{2.12}$$

Assuming $\Omega_g \gg \Omega_k$, the gravitational frequency dominates, so that $|u_n| \gg |v_n|$ and all precession frequencies $\Omega \approx \Omega_g$. Because $|u_n| \gg |v_n|$, we may use equation Eqn. 2.12 to find an equation for v_n in terms of u_n: $v_n \approx -\frac{\Omega_k}{4\Omega_g}\sum(u_n - u_m)e^{-2i\theta_{nm}}$, where the sum is over all neighbors m of gyroscope n. We note that this term is the origin of the next-nearest neighbor coupling connecting our system to the Haldane model.

When the result for v_n in terms of u_n is substituted into Eqn. 2.11, we obtain

$$\Omega u_n = \Omega_g u_n + \frac{\Omega_k}{2}\sum_m (u_n - u_m) - \frac{\Omega_k^2}{8\Omega_g}\sum_{mm'}(u_n - u_m)e^{2i\theta_{m'nm}} + \frac{\Omega_k^2}{8\Omega_g}\sum_{ml}(u_m - u_l)e^{2i\theta_{nml}}, \tag{2.13}$$

where $\theta_{nml} = \theta_{nm} - \theta_{lm}$ is the angle between the bonds nm and lm, the second to last sum is over all pairs of neighbors m and m' of n, and the last sum is over all neighbors m of n and neighbors l of m. Here, our last term corresponds to next-nearest neighbor coupling.

To compare directly with the topological Haldane model, we will analyze the lowest-order terms for the sums over the nearest neighbors and next-nearest neighbors:

$$\Omega u_n = \Omega_g u_n + \Omega_k \sum_m (u_n - u_m) + \frac{\Omega_k^2}{8\Omega_g}\sum_{ml}(u_m - u_l)e^{2i\theta_{nml}}. \tag{2.14}$$

Ω_k is similar to Haldane's nearest neighbor tunneling amplitude, t_1, and $\Omega_k^2/8\Omega_g$ is the next-nearest neighbor tunneling amplitude. As in Haldane's model, the next-nearest neighbor coupling terms have a complex exponential. In tight binding systems this phase factor is calculated using the Peierls substitution as $\theta = \int \vec{A} \cdot d\vec{\ell}$, where $d\vec{\ell}$ is along the tunneling path. In gyroscopic systems, the phase factor is governed purely by the lattice geometry.

The topological character of Haldane's system can be quantified by calculation of the Chern. A non-zero Chern number indicates a topologically non-trivial state and implies the existence of chiral edge currents. Systems with time reversal symmetry must have a Chern number equal to zero, as time reversal symmetry implies zero Berry curvature. However, not all systems with broken time reversal symmetry must have a non-zero Chern number. In general, two bands separated by a finite gap will not acquire non-zero Chern number because of infinitesimal perturbations.

However, an infinitesimal perturbation can produce a large change in Berry curvature at Dirac points. Therefore, even the small complex phase terms in the Haldane model and in eqn. Eqn. 2.13 can open a gap and induce a non-zero Chern number.

To see this effect mathematically, one can expand in powers of displacement from the Dirac point, $\vec{k}' = \vec{k} - \vec{k}_0$ (where $\vec{k}_0$ is the wavevector of the Dirac point). Then the hopping matrix, T, can be written in terms of Pauli matrices. For a system *without* next nearest neighbor coupling, we find that after rotating the wavevector, $\vec{k}' \to \vec{k}''$, the Hamiltonian can be written as: $H_{eff}(\vec{k}'') \sim k_x''\sigma_x + k_y''\sigma_y$. The Berry curvature of the two bands near this point are both zero. Terms with complex phases break the degeneracy between the two states, which can be represented by adding a term $m_{eff}\sigma_z$, where m_{eff} is an effective mass. Even if m_{eff} is small, this changes the Berry curvature very close to the Dirac point, so that the net curvature in the bottom band in the vicinity of the Dirac point is: $\int d^2k''\ \mathcal{F}_- = \pi$ sgn m_{eff}, and the band above the Dirac point has opposite curvature.

For the honeycomb lattice there are only two sites per unit cell, so there are two modes with each wave number. A basis can be obtained by defining $u = 1$ on one of the two sites and 0 on the other, and translating to other unit cells while multiplying by $e^{i\vec{k}\cdot\vec{x}}$ (Fig. 2.3). The degeneracy points are at $\vec{k}_0 = \pm(\frac{2\pi}{3a}, \frac{2\pi}{3\sqrt{3}a})$, where a is the edge length of the hexagon; Fig. 2.3 shows the two basis states near $\vec{k}_0 = (\frac{2\pi}{3a}, \frac{2\pi}{3\sqrt{3}a})$.

Let us focus on Eqn. 2.14 and the terms which arise from hopping along the diagonals (next-nearest neighbors, u_l; see Fig. 2.4), since these are the terms which produce a gap. The matrix for the hopping along the sides is, to lowest order in $\vec{k}''$: $\frac{3}{2}at_1(k_x''\sigma_x + k_y''\sigma_y)$, where $t_1 = \Omega_k$ is the nearest neighbor hopping amplitude. To understand the contribution from the next-nearest neighbor hopping, we set $\vec{k}'' = 0$. As shown in Fig. 2.3, the two basis wave-functions now resemble vortices circulating around the hexagons in opposite directions.

Both wave-functions pick up the same phase under translation, but they transform oppositely under rotation. Because the phase differences are different, the energies (i.e., frequencies of the normal modes in the gyroscope system) of the states are different; the one whose phase shifts match the phase of the hopping better has the lower energy (i.e. the energies are $-2t_2\sum_{r=1}^{3}\cos(\phi_{2r} - \frac{2\pi}{3})$ and $-2t_2\sum_{r=1}^{3}\cos(\phi_{2r-1} + \frac{2\pi}{3})$, where $t_2 = \frac{\Omega_k^2}{8\Omega_g}$ and $\phi_r = 2\theta_{nml}$ for the r next-nearest neighbors).

If we include the energy splitting and the linear terms in $\vec{k}'$, we have:

$$H(\vec{k}'') = \frac{3}{2}at_1(\pm k_x''\sigma_x + k_y''\sigma_y) \underbrace{-t_2 \sum_{r=1}^{6}(-1)^r \cos\left(\phi_r \pm (-1)^r \frac{2\pi}{3}\right)}_{m_{eff}=\frac{t_2}{2}\sum_r[(-1)^r\cos\phi_r \mp \sqrt{3}\sin\phi_r]} \sigma_z, \tag{2.15}$$

where the top sign refers to the Dirac point we have been considering and the bottom sign is for the other one. If the phase-shifts have 2-fold symmetry, i.e. $\phi_{r+3} = \phi_r$, we can simplify the effective mass to: $m_{eff} = \mp\frac{\sqrt{3}}{2}t_2 \sum_r \sin\phi_r$

The total Berry curvature for each of the two Dirac points is: $\int d^2k''\, \mathcal{F}_- = \mp\pi \text{ sgn } m_{eff} = \pi \text{ sgn}\,[\sum_r \sin\phi_r]$. As a result, the Chern number of the top/bottom band is given by: $C_\pm = \pm\text{sgn}\,[\sum_r \sin\phi_r]$

In general, distorting the honeycomb lattice produces different phase shifts along different diagonals (Fig. 2.4). For a distorted honeycomb lattice, there are four angles of the hexagon equal to α and two equal to $2\pi - 2\alpha$. The phases are twice this; thus the Berry curvature near each Dirac point is $\int d^2k''\, \mathcal{F}_- = \pi \text{ sgn}\,[2\sin(4\alpha) - 4\sin(2\alpha)]$. This curvature, and hence the Chern number, switch sign when the hexagon is distorted into a rectangle.

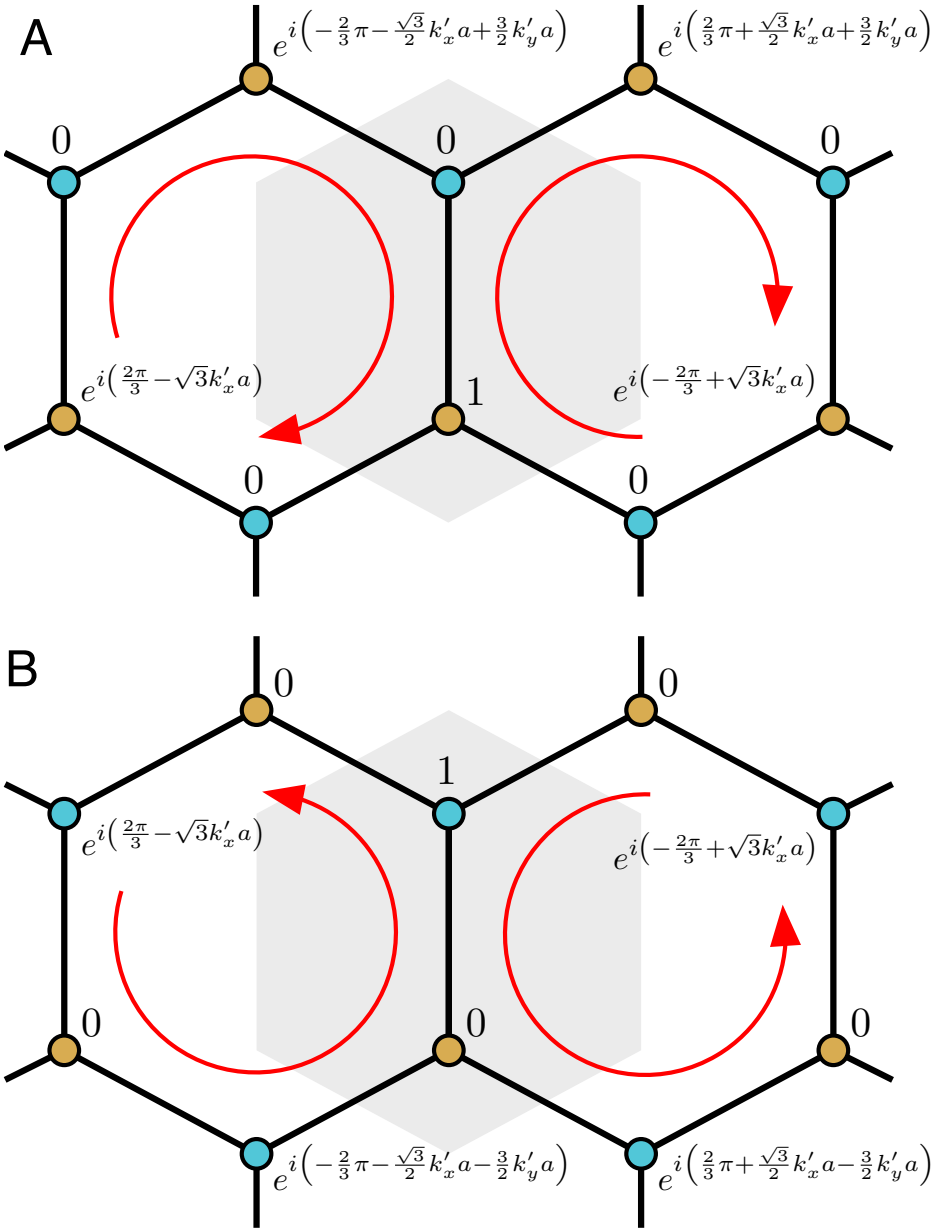

Figure 2.3: *The two basis wave functions for near a Dirac point.* The two basis wave functions for near the Dirac point at $\vec{k}_0 = (\frac{2\pi}{3a}, -\frac{2\pi}{3\sqrt{3}a})$, as a function of displacement from the Dirac point: $\vec{k}' = \vec{k} - \vec{k}_0$. The bases are generated by starting with an arbitrary wave function in a unit cell (indicated with the shaded hexagon), and then repeating the wave-function periodically, with wave-vector induced phase factors. One of the wave functions has an angular momentum of +1 around a hexagon and the other has an angular momentum of -1 around a hexagon, as indicated with the red arrows.

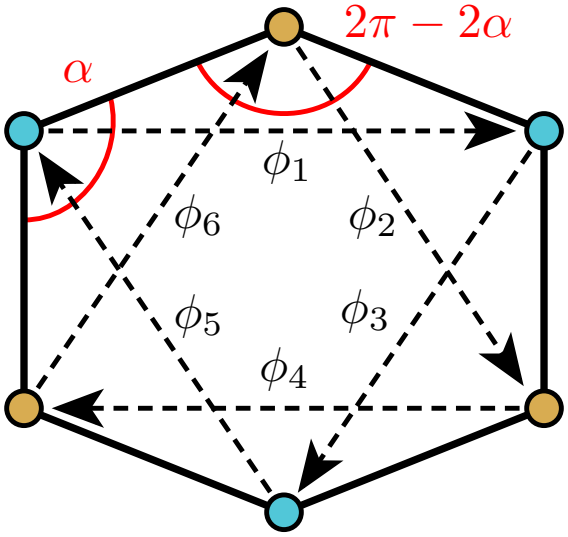

Figure 2.4: *Phase shifts for next-nearest neighbor hoppings.* Although these phase shifts are equal for a hexagon, distorting the lattice will make the phase shifts non-uniform. In general, adding diagonal hopping terms (dotted arrows) opens gaps at the Dirac points.

CHAPTER 3

GYROSCOPIC METAMATERIALS IN SIMULATION AND EXPERIMENT

3.1 Introduction

A vast range of mechanical structures, including bridges, covalent glasses and conventional metamaterials can be ultimately modeled as networks of masses connected by springs [11, 12, 13, 14, 15, 16]. Recent studies have revealed that despite its apparent simplicity, this minimal setup is sufficient to construct topologically protected mechanical states [6, 7, 17, 18] that mimic the properties of their quantum analogues [3]. This follows from the fact that, irrespective of its classical or quantum nature, a periodic material with a gapped spectrum of excitations can display topological behavior as a result of the non-trivial topology of its band structure [5, 19, 20, 21, 22, 23, 24, 25, 26].

All such mechanical systems, however, are invariant under time reversal because their dynamics are governed by Newton's second law, which, unlike the Schrödinger equation, is second order in time. If time reversal symmetry is broken, as in recently suggested acoustic structures containing circulating fluids [21], theoretical work [5] has suggested that phononic chiral topological edge states which act as unidirectional waveguides resistant to scattering off impurities could be supported.

Here we show that by creating a coupled system of gyroscopes, a 'gyroscopic metamaterial', we can produce an effective material with intrinsic time reversal symmetry breaking. As a result, our gyroscopic metamaterials support topological mechanical modes analogous to quantum Hall systems, which have robust chiral edge states [4, 27, 28]. We demonstrate these effects by building a real system of gyroscopes coupled in a honeycomb lattice. Our experiments show long-lived, unidirectional transport along the edge, even in the presence of significant defects. Moreover, our theoretical analysis indicates that direction of edge propagation is controlled both by the gyroscope spin and the geometry of the underlying

lattice. As a result, deforming the lattice of gyroscopes allows one to control the edge mode direction, offering unique opportunities for engineering novel materials.

3.2 Results on the Honeycomb Lattice

Much of the counterintuitive behavior of rapidly spinning objects originates from their large angular momentum, which endows the axis of spin with a resistance to change. If we fix one end of a gyroscope and apply a force, $\vec{F}$, to the opposing free end of the spinning axis, we produce a torque of $\vec{\tau} = \vec{\ell} \times \vec{F}$, where $\vec{\ell}$ is the axis of the gyroscope, pointing from the fixed to the free end. In the fast spinning limit, the response of the gyroscope's axis is:

$$\dot{\vec{\ell}} = \frac{\ell^2}{I\omega}(\hat{\ell} \times \vec{F}) \tag{3.1}$$

where ω is the gyroscope angular frequency and I is its rotational inertia. The behavior of a gyroscope differs from that of a simple mass in two important ways: (i) it moves perpendicular to applied forces and (ii) its response is first order in time. The canonical example of this unusual behavior is precession: a spinning top does not simply fall over, but rather its free end orbits around the contact point (precesses) with a constant period, $\Omega_g = \frac{mg\ell_{cm}}{I\omega}$, where ℓ_{cm} is the distance from the pivot point to center of gravity.

What happens if we replace the masses in a conventional mechanical metamaterial with gyroscopes? A first glimpse is provided by a normal mode analysis of honeycomb lattices composed of mass-spring and gyroscope-spring networks. The density of states of these two systems (Fig. 3.1A) show qualitatively similar features: each is characterized by two bands: a lower 'acoustic' band (where neighboring sites move in phase) and an upper 'optical' band (where neighboring sites move out of phase). The connections between these two bands, however, show key differences: in the mass-spring system the two bands touch at a Dirac point, while in the gyroscopic system a gap opens up between the bands. Crucially, this gap is not empty, but populated by nearly equally spaced modes and the number of these edge

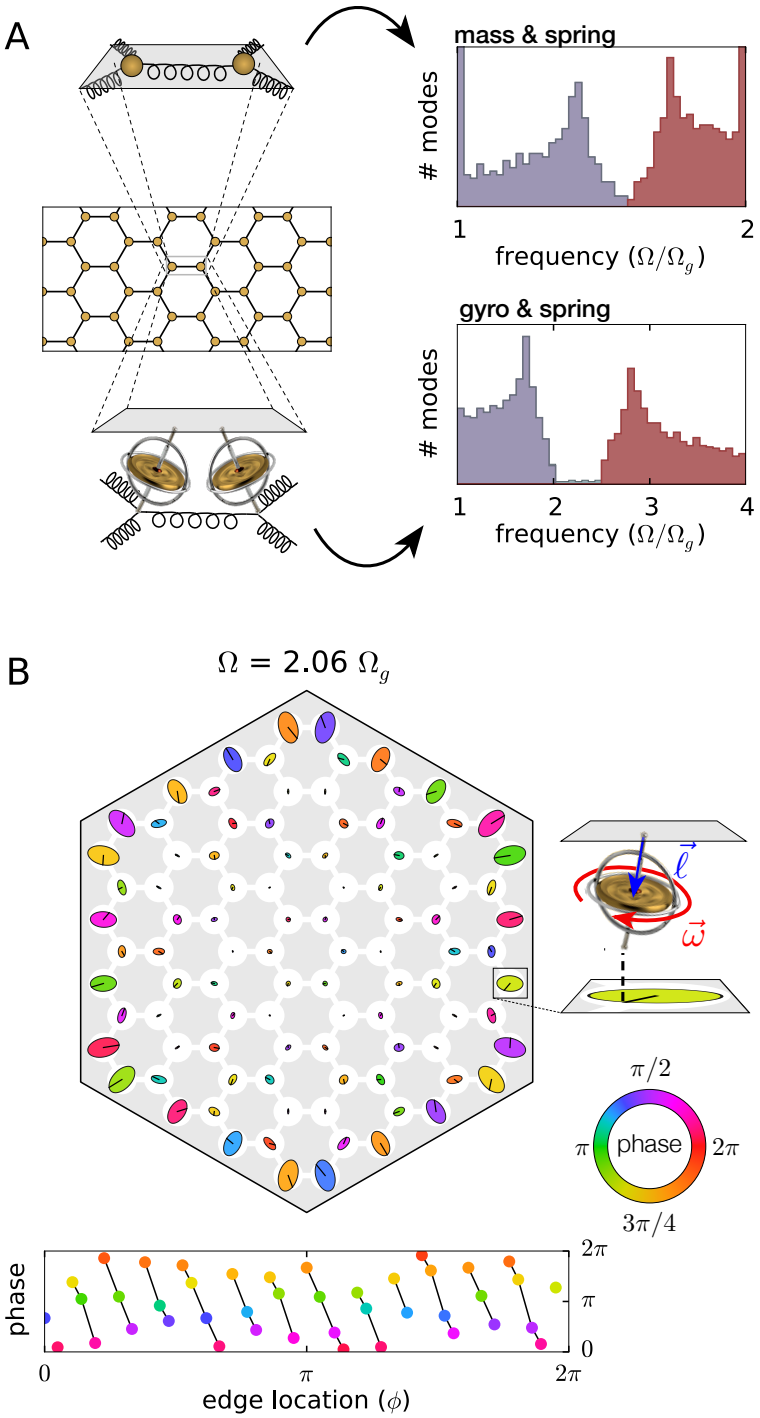

Figure 3.1: *Gyroscopic metamaterials and computational edge states.* *(A)* A comparison between the density of states of a mass-spring (top) and gyroscopic metamaterial (bottom) on a honeycomb lattice. In the network of gyroscopes, there is a gap between acoustic and optical bands which is populated by chiral edge modes. *(B)* A normal mode between the acoustic and optical bands in a lattice of 96 gyroscopes. The shape of each orbit in the normal mode is indicated with ellipses and the phase at a fixed time is indicated via color.

modes scales with the length of the edge. Examination of these gap modes reveals them to be confined to the edge and to be chiral: the phases always rotate in the same direction as one moves around the lattice (Fig. 3.1B). As we show below, these edge modes are topologically robust and can therefore serve as unidirectional waveguides.

It is far from obvious that in a real system the phonon spectrum would be resistant to the presence of both disorder (lattice imperfections, gyroscopic non-uniformity, etc.) and mixed-order dynamics (e.g. nutation). On the other hand, an appealing feature of topological states is that they are often resistant to disorder, suggesting that they may be useful for acoustic applications and observable under a wide range of experimental conditions.

To explore the relevance of these effects, we have assembled a prototype system of 54 interacting gyroscopes on a honeycomb lattice, Fig. 3.3A, Fig. 3.2. Our gyroscopes consist of small DC motors spinning cylindrical masses at $\sim$300 Hz (with $\sim 10\%$ variation in motor speed); each is suspended from a top plate by a weak spring, Fig. 3.3B, producing an individual precession frequency of $\Omega_g \sim 1$ Hz. To couple these gyroscopes in a lattice, a small neodymium magnet is placed in each spinning mass, with its moment aligned vertically causing the gyroscopes to repel. For small displacements, this creates a linear effective spring-like force between gyroscopes which is comparable in strength to the gravitational pinning force.

The magnetically coupled system is conceptually equivalent to the system of gyrosocopes connected by springs discussed earlier; the linearized magnetic coupling differs however in detail from the coupling given by springs since the equilibrium results from the cancellation of opposing forces instead of the absence of forces. As detailed in the supporting information, this results in a mode spectrum which is shifted to lower frequencies, Fig. 3.3C, when compared to a spring-coupled gyroscope system, Fig. 3.1A. However, the topological character of the band-structure is not affected and acoustic and optical bands are still apparent with chiral edge modes in between.

To test the mechanical response of the gyroscopic metamaterial, we excite it with periodic

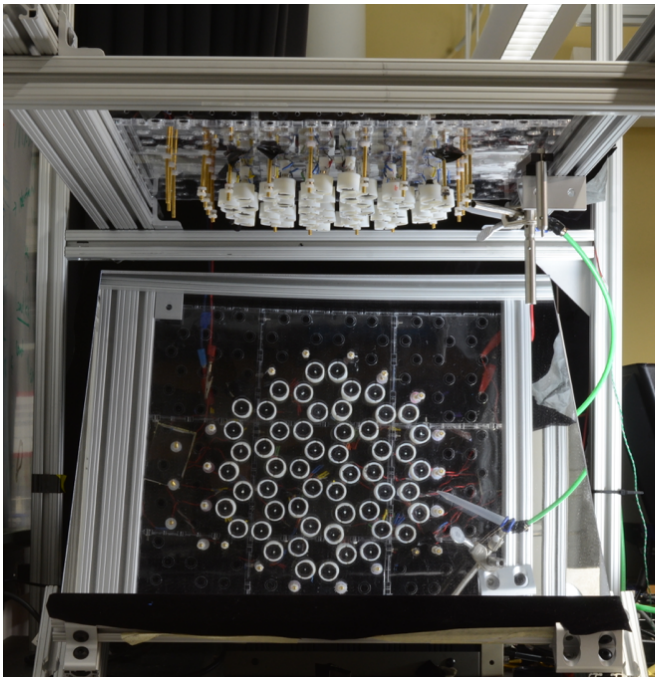

Figure 3.2: *Experimental gyroscopic metamaterial set-up* The gyroscopic metamaterial is composed of 54 gyroscopes suspended from an acrylic plate by springs and coupled by magnetic dipole interactions.

bursts of air through a small nozzle, and follow the resulting disturbance. We probe the normal modes by weakly exciting a single gyroscope at a fixed frequency for many (> 100) periods, and recording the resulting motion of the network. All excitations were kept to small amplitudes ($< 10\%$ of the lattice spacing) to avoid the non-linearities associated with coupling the gyroscopes magnetically.

The effect of disorder inherent to our experiment (e.g. variation in motor speed and gyroscope pivot position) can be clearly seen in the comparison between the structure of bulk modes as shown in Fig. 3.3 D&F for the idealized (left) and experimental system (right). There is little overall agreement between calculated and measured modes, though acoustic modes show approximate in phase oscillation of adjacent gyroscopes and optical modes show approximate out of phase oscillation of adjacent gyroscopes. This is characteristic of the effects of disorder [29], which produces the same effect in numerically evaluated modes with comparable disorder, Fig. 3.4.

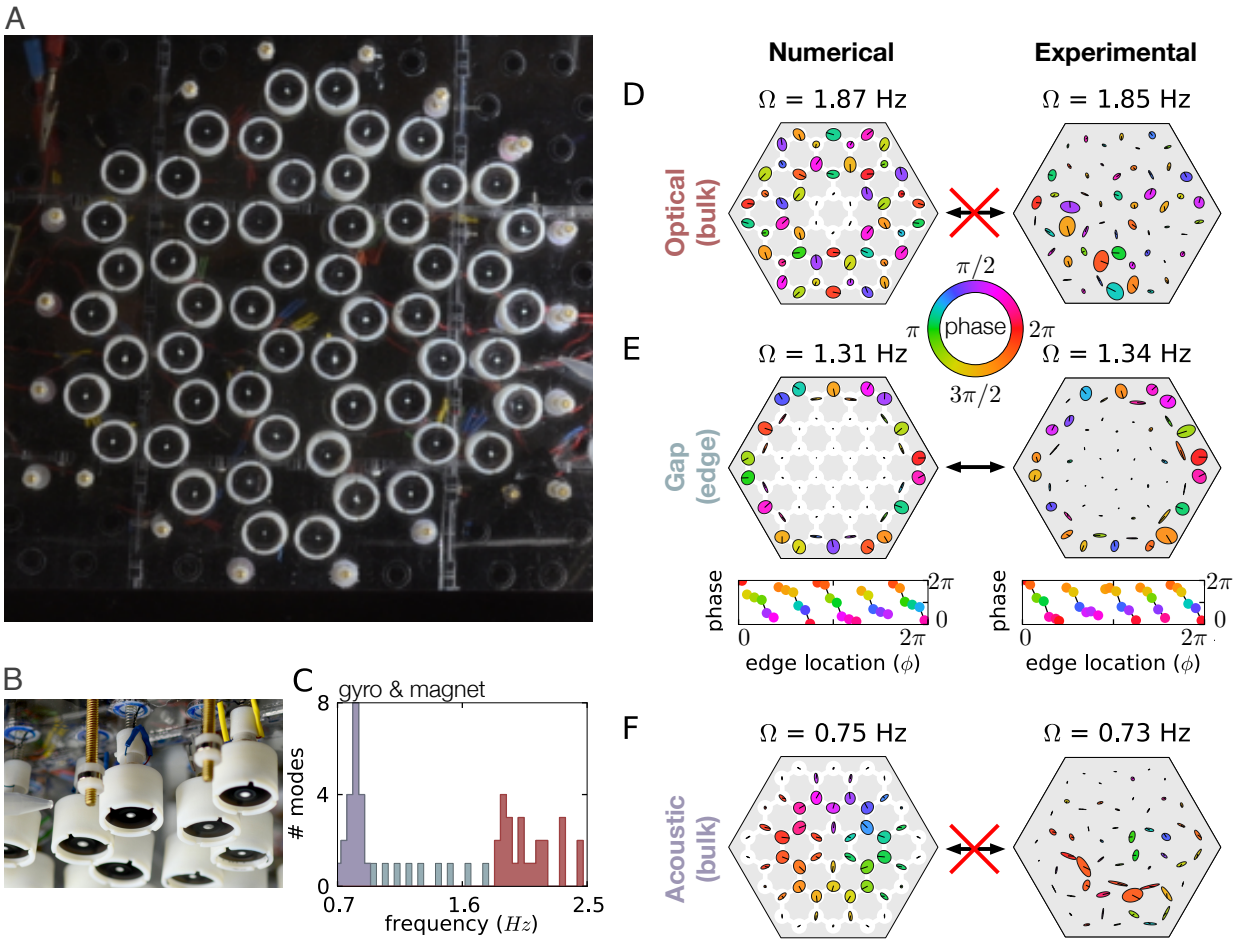

Figure 3.3: *Demonstration of robustness of edge modes in experiment.* *(A)* A picture of the experimental system as viewed from below. *(B)* The edge of the experimental lattice from the side, showing the construction of the individual gyroscopes as well as the fixed magnets around the edge that provide the lateral confinement. *(C)* The calculated histogram of normal mode frequencies for an array of 54 gyroscopes arranged in a honeycomb lattice (no disorder) is shown. The frequencies range from 0.7-2.5 Hz. Panels *(D-F)* show a comparison of calculated normal modes in an ideal magnetic-gyroscope network (left) as measured in an experimental system (right) For each system a mode is shown in *(D)* the optical band, *(E)* the bandgap, and *(F)* the acoustic band. Disorder has a strong effect on bulk mode profiles. However, the gap mode profiles correspond much more closely to the ideal modes in shape, orientation, and phase of the gyroscope orbits.

Despite these experimental imperfections, exciting a mode in the gap between the acoustic and optical bands produces clean excitations along the edge, Fig. 3.3E. The orientations and relative orbit sizes of these modes closely match the modes numerically computed for an idealized model. A comparison between calculated and measured edge mode frequencies is shown in Fig. 3.5. The robustness of these modes against disorder is characteristic of their topological character.

To demonstrate that our experimental metamaterial functions as a unidirectional waveguide, we excite a single edge gyroscope for five periods at a frequency in the gap. As shown in Fig. 3.6A, the resulting excitation propagates in only one direction around the edge of the lattice. The motion of this wave packet around the edge is persistent, circumnavigating the boundary several times. As expected, short excitations at a frequency not in the band gap do not produce a similar robust edge excitation. Crucially, this indicates that the chiral edge modes are topologically protected from coupling to the bulk modes, functioning as an efficient one-directional waveguide.

We further demonstrate the robustness of these edge modes by intentionally introducing disorder in the lattice, for example, by removing three gyroscopes. As shown in Fig. 3.6B, even this significant disturbance does not destroy the chiral edge modes. An excitation on the edge is seen to move around this disturbance – in the same direction as before – and emerge undisturbed on the other side. Remarkably, the excitation traverses the defect region without scattering backwards or into the bulk. As before, the resilience of the edge modes suggests these edge states are topological in character.

To analyze the origin of these effects, we return to an ideal coupled gyroscope model.

As previously derived, the linearized equation of motion for each site in the gyroscopic metamaterial is:

$$i\frac{d\psi_p}{dt} = \Omega_g\psi_p + \frac{1}{2}\sum_{q\,\in\,n.n.(p)}\Big[\left(\Omega^+_{pp}\psi_p + \Omega^+_{pq}\psi_q\right) + e^{2i\theta_{pq}}\left(\Omega^-_{pp}\psi^*_p + \Omega^-_{pq}\psi^*_q\right)\Big], \tag{3.2}$$

where p is the site label, q the neighboring sites, θ_{pq} is the spring bond-angle, and $\Omega^{\pm}_{pj} = -\frac{\ell^2}{I\omega}(\frac{\partial F_{p\parallel}}{\partial x_{j\parallel}} \pm \frac{\partial F_{p\perp}}{\partial x_{j\perp}})$ are determined from gradients of the force on p, F_p, parallel and perpendicular to the line connecting the equilibrium positions of the gyroscopes. In the case of the interactions being provided by springs, $\Omega^{\pm}_{pq} = \frac{k\ell^2}{I\omega} = \Omega_k$, where k is the spring constant.

We analyze the breaking of temporal symmetry using the 'time-reversal' operation in quantum mechanics: $t \to -t$, $\psi \to \psi^*$. For gyroscopes, conjugating ψ mirrors their displacement in the y-axis; applying the complete time-reversal operation to a single gyroscope leaves the equation of motion unchanged. Similarly, for a network of gyroscopes Eqn. 3.3 is invariant under this operation only if the coefficient $e^{2i\theta_{pq}}$ is real (up to a global rotation), and breaks the symmetry otherwise. Thus, we again see that the breaking of time reversal symmetry depends on distribution of bond angles in the lattice, and not simply the response of individual gyroscopes.

The geometric origin of the time reversal symmetry can also be seen in the case of gyroscopes connected by springs, by considering the energy of two connected gyroscopes. In the linearized limit, the stretching/compression of the spring is given by: $\Delta \propto (r_{x1} - r_{x2})\cos\theta_{12} + \left(r_{y1} - r_{y2}\right)\sin\theta_{12}$. If we mirror each gyroscope in the y-axis ($\psi \to \psi^*$ or $r_y \to -r_y$), in general the spring length will be unchanged only if $\sin\theta_{12} = 0$, i.e. if the mirror axis aligns with the equilibrium bond angle. However, if $\cos\theta_{12} = 0$, or the mirroring axis is perpendicular to the bond, then the spring energy, $E_k \propto \Delta^2$, is conserved by converting stretching to compression (Fig. 3.7A). When considering an entire lattice, we see that for arbitrary displacements the bond energy will be conserved under time-reversal if (and only if) we are

able to choose a global mirror axis to which all bonds are either perpendicular or parallel. As a result, time-reversal invariance is only guaranteed for lattices composed of square or rectangular building blocks.

As detailed in section 2.4, in the limit that gyroscopes are coupled by weak springs, $\Omega_k \ll \Omega_g$ our gyroscopic metamaterial has a well-known quantum-mechanical analog: the Haldane model of an electronic system in a honeycomb lattice [2]. In the Haldane model, time reversal symmetry is broken by a staggered magnetic field. This field can be varied, resulting in a change in the topological character of the modes as quantified by the Chern number [9, 30, 3]. Accordingly, depending on the strength of the field and asymmetry between the two sites in the unit cell, the Chern number of the bottom band is $C_- = 0, \pm 1$, and $C_+ = -C_-$ in the top band. A Chern number of zero indicates a trivial topology (a normal insulator) while a non-zero Chern number indicates a non-trivial topology. Whenever $C_\pm \neq 0$, topological edge modes appear in the gap between the two bands; the chirality and direction of propagation of these modes depends on the sign of the Chern number for lower band.

In gyroscopic metamaterials, the analogue to changing the magnetic field is to geometrically distort the lattice. In either case, the relevant operation produces a phase-shift in the hopping between neighboring sites; in the gyroscope system this phase shift is determined by the bond angles, θ_{pq}. In the case of an undistorted honeycomb lattice, the modes have a Chern number of $C_\pm = \pm 1$, in agreement with the Haldane model.

In a honeycomb lattice, it is possible to distort the constituent hexagons without changing the bond length (Fig. 3.7B-D), allowing us to change the gyroscopic phase between neighboring sites without changing the network connectivity. As predicted by the time-reversal analysis above, the band-gap and chiral edge modes disappear when the bonds fall on a rectangular grid (in which case $e^{2i\theta_{pq}} = \pm 1$). Furthermore, the dispersion relationship of an infinite gyroscopic lattice in this configuration has Dirac points at the corners of the Brillouin zone (Fig. 3.7C); this is topologically equivalent to the dispersion relationship of a

honeycomb network of springs and masses. Continuing to distort the lattice past this point restores the band-gap, but the edge modes now have *opposite* chirality, as reflected in an inversion of the bands and hence of the Chern number; $C_{\pm} = \mp 1$. As a result, excitations along the edge now move in the other direction, opposite to the precession of individual gyroscopes. Simulations show that the edge mode direction can be switched during propagation if the metamaterial is continuously distorted. Remarkably, this indicates the direction of the edge wave-guide can be controlled purely through geometric distortions of the lattice, analogous to an effect recently observed in 1D acoustic phononic crystals [31].

3.3 Details of the magnetic interaction

In the experiment the energy minimum at the equilibrium positions is created by the cancellation of opposing forces rather than the absence of forces. Magnetically coupled gyroscopes are a specific instance of coupling with a general radial interaction force, $\vec{F} = F(r)\hat{r}$. In these cases, we find the effective spring constants (and therefore the effective coupling precession frequencies) by taking the coefficients of the first derivatives of the interaction force. For a radially symmetric potential of the form $\vec{F}(r) = kr^n\hat{r}$, this results in $\Omega_p^{\pm} = \frac{k\ell^2}{I\omega}\,(n \pm 1)\,a^{n-1}$ and $\Omega_q^{\pm} = -\Omega_p^{\pm}$, where a is the separation between the two lattice sites.

In this case, we obtain the following equation of motion:

$$i\frac{d\psi_p}{dt} = \Omega_g\psi_p + \frac{1}{2}\sum_q^{n.n.}\Big[\left(\Omega_p^+\psi_p + \Omega_q^+\psi_q\right) + e^{2i\theta_{pq}}\left(\Omega_p^-\psi_p^* + \Omega_q^-\psi_q^*\right)\Big], \tag{3.3}$$

where $\Omega_j^{\pm} = -\frac{\ell^2}{I\omega}(\frac{\partial F_{p\parallel}}{\partial x_{j\parallel}} \pm \frac{\partial F_{p\perp}}{\partial x_{j\perp}})$.

In our experiment, the gyroscopes are coupled through small magnets. The force can be approximated by treating each gyroscope as a magnetic dipole with strength M; this produces an r^{-4} radial force between the gyroscopes plus an anti-restoring torque from the

magnetic interaction. The total effective force gradients are given by:

$$\begin{aligned} \frac{\partial F_{p\|}}{\partial x_{p\|}} &= -k_m\left(1-\frac{a^2}{12\ell^2}\right); \quad \frac{\partial F_{p\|}}{\partial x_{q\|}} = +k_m\left(1+\frac{a^2}{6\ell^2}\right) \\ \frac{\partial F_{p\perp}}{\partial x_{p\perp}} &= +\frac{k_m}{4}\left(1+\frac{a^2}{3\ell^2}\right); \quad \frac{\partial F_{p\perp}}{\partial x_{q\perp}} = -\frac{k_m}{4}\left(1+\frac{a^2}{3\ell^2}\right) \end{aligned} \tag{3.4}$$

where $k_m = \frac{3\mu_0 M^2}{\pi a^5}$ is the magnetic characteristic spring constant, corresponding to a gyroscope precession frequency of $\Omega_m = \frac{k_m \ell^2}{I\omega}$, and we have converted torques between the magnetic dipoles to equivalent forces which depend on the ratio of lattice spacing (a) to pendulum length (ℓ).

In a honeycomb lattice, the symmetry of the lattice allows for the equations of motion to be simplified to:

$$\begin{aligned} i\frac{d\psi_p}{dt} = \Omega_g'\psi_p + \frac{1}{2}\sum_q^{n.n.}\Big[&\Omega^+\left(\psi_p - \psi_q\right) + \\ &\Omega^- e^{2i\theta_{pq}}\left(\psi_p^* - \psi_q^*\right)\Big], \end{aligned} \tag{3.5}$$

where $\Omega_g' = \Omega_g - \frac{3a^2}{8\ell^2}\Omega_m$ and $\Omega^\pm = \left[1+\frac{a^2}{6\ell^2} \mp \left(\frac{1}{4}+\frac{a^2}{12\ell^2}\right)\right]\Omega_m$. Here we see that the magnetically coupled system is different from the spring coupled lattice in two ways: the effective pinning frequency, Ω_g is decreased, and there is an asymmetry between the Ω^+ and the Ω^- terms.

The equation of motion for the magnets, Eqn. 3.5, is nearly equivalent to the simple linear spring case, excepting the slight asymmetry between the ψ and ψ^* terms. (Note that for springs, the *pairwise* force between the two sites is 0 at equilibrium, which results in $\Omega_p^\pm = \Omega_k$ and $\Omega_q^\pm = -\Omega_k$ and recovers a simpler equation of motion, Eqn. 2.6.) The asymmetry of these terms has an interesting effect when viewed from the perspective of time reversal symmetry breaking: the ψ^* terms couple forward and backward propagating modes, and so when $\Omega_- > \Omega_+$ the symmetry breaking terms are relatively stronger. As a result there is a wider bandgap for the magnetically coupled gyroscopes in comparison to those

coupled by linear springs.

3.4 Conclusions

This work was the first experimental proof of concept and theoretical analysis of a topologically protected unidirectional waveguide in a real mechanical metamaterial. Analysis indicates that our topological edge modes arise from the combination of the chiral nature of the gyroscopes and the geometry of the underlying lattice. Because the direction of the edge modes can be changed discontinuously with geometric distortions, in principle small displacements should be capable of inverting the edge mode direction. This mechanism may have practical applications for creating direction-tunable materials, but it also suggests interesting non-linear effects should occur in the regime near the mechanically-induced topological phase transition.

The prototypical gyroscopic material we developed is an example of an active metamaterials: its design relies on the presence of internal motors that keep each gyroscope in a fast spinning state. An open challenge is to construct scalable gyroscopic metamaterials using nano-fabrication techniques (e.g. MEMS) or active molecules that convert chemical energy into rotation very much like the motors powering each gyroscope [32, 33]. Such an implementation would pave the way towards realizing materials that support, at a microscopic scale, robust topological acoustic modes.

Though we gained significant insight into the properties of lattice gyroscopic materials, an important question remains largely unexplored: What are the requirements for topology in a gyroscopic metamaterial? In the next few chapters, we explore requirements for topology in gyroscopic lattices and extend to amorphous networks.

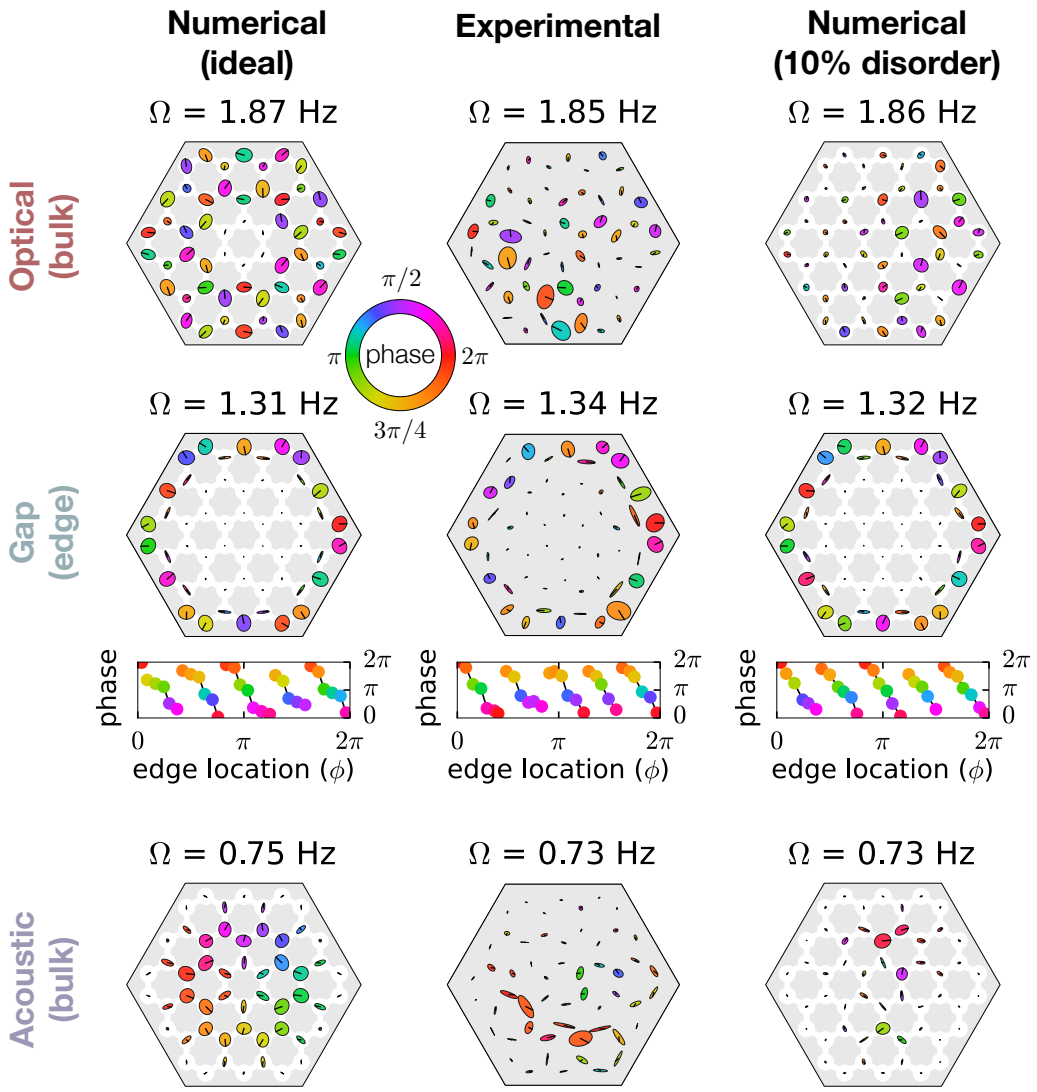

Figure 3.4: *Comparison between ideal numerical modes, experimental modes, and numerically calculated modes with 10% disorder.* The effect of random disorder on mode profiles is qualitatively similar to the mode profiles observed in the experimental system, which had a similar amount of disorder.

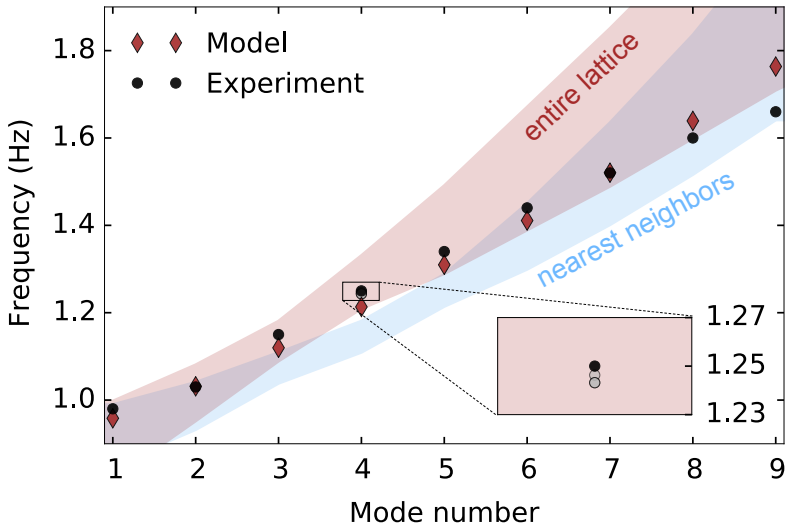

Figure 3.5: *A comparison between the experiment and magnetic model for gap mode frequencies.* The red (blue) shaded region indicates the possible values of gap mode frequencies for mode numbers 1–9 from calculations using measured m and ℓ values with entire lattice (nearest neighbor) coupling. Mode numbers 1–9 are observed in the experiment with a gap extending from $\sim 1 - 1.7$ Hz. Modes 8 and 9 show some mixing with bulk modes. The diamonds show values for a theoretical model with $M = 0.21$ Am^2 and $\ell = 38$ mm, corresponding to $\Omega_m = 0.86$ Hz (with entire lattice coupling). For this system, $\Omega_g = 0.98$ Hz, which was determined by measuring a single gyroscope. The inset shows the change in frequency observed when the mode amplitude is increased from $1.2 - 4.0$ mm (measured as the largest displacement of a single gyroscope).

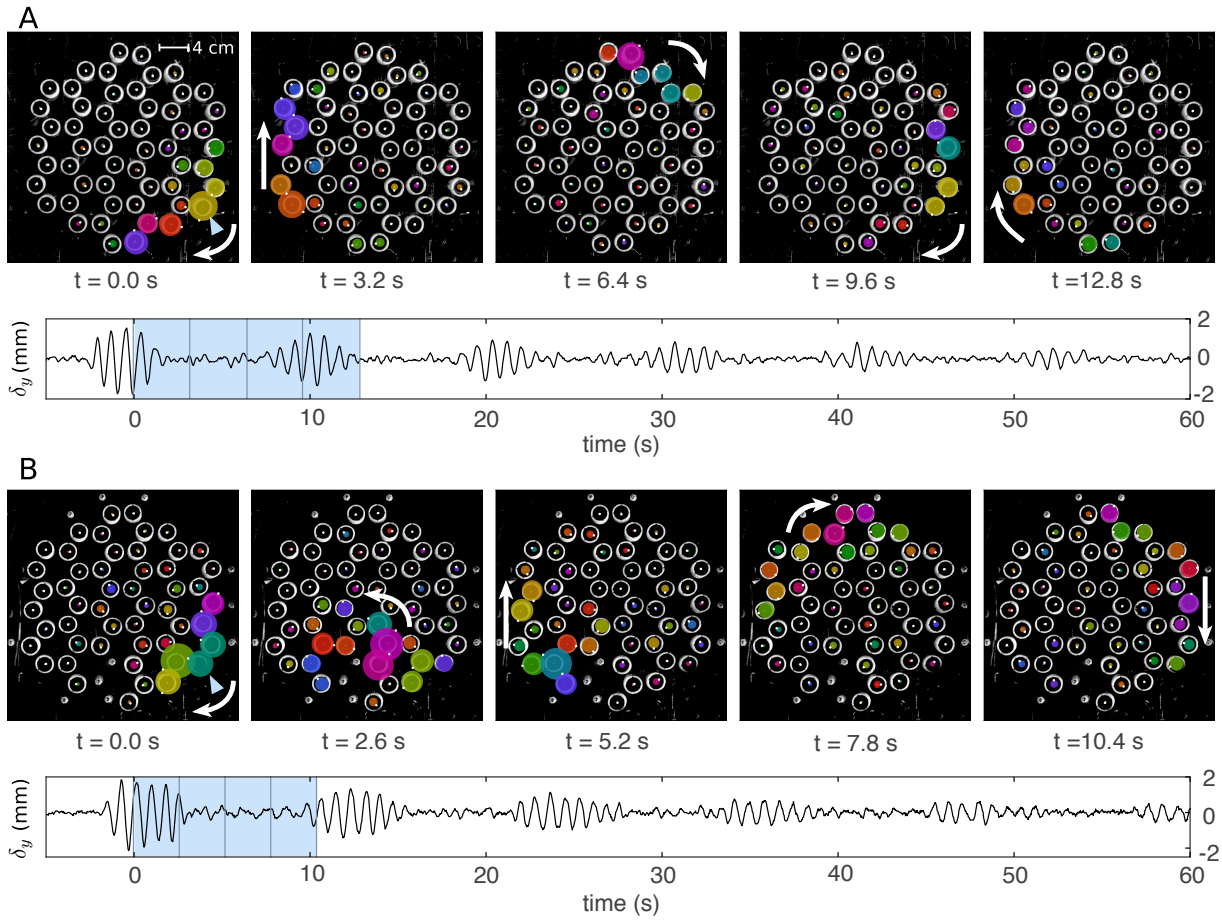

Figure 3.6: *Unidirectional waveguide modes in experiment. (A)* A single edge gyroscope is excited for five periods; subsequent images show the excitation propagation clockwise around the edge. The bottom graph indicates the displacement of one gyroscope (indicated with a triangle) in the y-direction; the excitation is seen to persist for many cycles around the edge. *(B)* The same experiment as in *(A)*, but with three gyroscopes removed from the bottom edge and replaced with fixed magnets (to keep the system in equilibrium). Due to the topological nature of the edge modes, the excitation propagates around the disturbance.

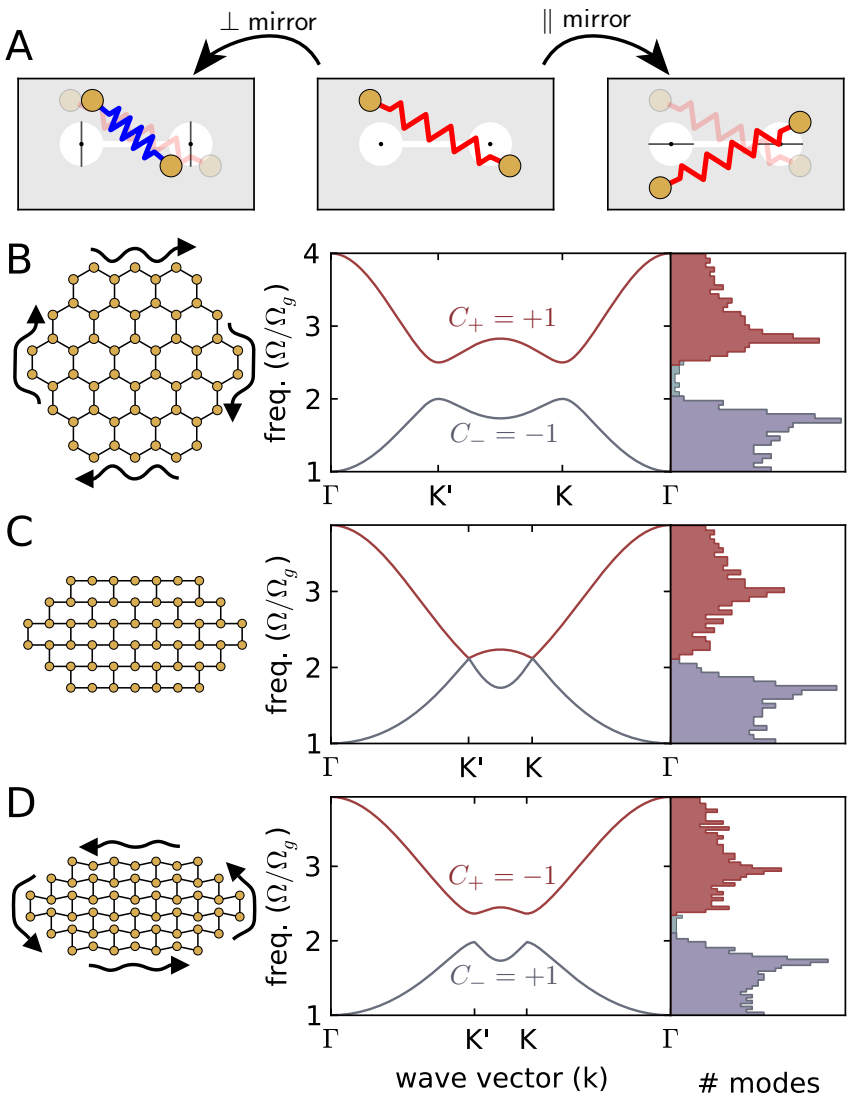

Figure 3.7: *Controlling time-reversal invariance in a gyroscopic metamaterial. (A)* The effect of mirroring a configuration of two gyroscopes around axes which are perpendicular or parallel to the equilibrium bond angle. Mirroring about axes that are perpendicular to the bond angle (left) converts stretching to compression but conserves the energy stored in the bond. Mirroring about the axes that are parallel to the bond (right) conserves the total bond length. Mirroring about other axes, in general, does not conserve energy. *(B-D)* For each lattice geometry (shown at left), the band structure for an infinite system is shown (middle) along with the density of states for a finite lattice of 726 gyroscopes (right). *(B)* shows an undisturbed, hexagonal honeycomb lattice. *(C)* shows a honeycomb lattice as it is distorted into a rectangular configuration while preserving the connectivity, and *(D)* shows a honeycomb lattice distorted past the square configuration. The rectangular configuration has no bandgap, and consequently no edge modes; as the lattice is further distorted the bandgap reopens but the edge modes have opposite chirality.

CHAPTER 4

LATTICE PROPERTIES AND TOPOLOGY

4.1 Introduction

Materials with nontrivial band topology have captured the attention of condensed matter scientists since the discovery of the quantum Hall effect in 1980 [34]. Though many models of topological matter have been proposed since, these systems all share common characteristics: they are insulating in their bulk and have edge states which are insensitive to disorder [3]. Recent studies have additionally shown that nontrivial band topologies exist not only in the quantum mechanical regime, but also in several classical photonic, acoustic, and even mechanical systems [23, 21, 35, 6, 24, 36, 27, 26, 25, 17, 37, 28, 38, 5, 39].

Similarly to their electronic counterparts, phononic excitations of mechanical metamaterials have a rich classification structure based on symmetries [8]. A class that breaks time reversal symmetry exhibits excitations which can propagate around a boundary in one direction. In mechanical systems, this feature promises applications in the design of one-way acoustic waveguides and has recently been demonstrated using structures composed of coupled gyroscopes [37, 35].

Previous studies of topological gyroscopic materials have focused only on specific lattices [37, 35]. However, in order to effectively engineer one-way waveguides with these materials it is crucial that we understand topology in a broader context. Here we provide insights into gyroscopic topology through a study of the roles of lattice geometry and type, site equivalence, and coordination number. We find that nontrivial band topology is general across many gyroscopic lattices. Building on our observations, we offer a simple prescription for constructing lattices with topological excitations.

4.2 Time reversal symmetry and topological band-gaps

In the previous chapter, breaking time reversal symmetry was the essential ingredient in ensuring nontrivial topology the gyroscopic honeycomb lattice. Now we ask if breaking time reversal symmetry is a sufficient condition with all other symmetries intact in gyroscopic materials.

In the honeycomb lattice, we can tune time reversal symmetry by changing the geometry via bond-length preserving deformations. As shown in Fig. 4.2(A), changing a lattice angle, δ, takes us through a topological phase transition. As δ passes through 180°, edge modes change direction and the Chern number changes sign [37]. Now we explore the entire phase-space of bond-length preserving deformations by introducing an additional angle ϕ, also depicted in Fig. 4.2(A).

In the resulting topological phase diagram, Fig. 4.2(B), red (blue) correspond to a Chern number of 1 (-1) and clockwise (counter-clockwise) propagating modes. The transition studied in [37] lies along the line $\phi = 0^\circ$. As should be expected, the penetration depth of edge modes diverges as the band gap closes, Fig. 4.1

Precisely at the transition point, time reversal symmetry is restored and the band-gap closes. At the transition, the network is arranged in a 'brick-layer' lattice, where $\delta = 180^\circ$ and $\phi = 0^\circ$ (Fig. 4.2(C)). Varying ϕ at the this transition point breaks time reversal symmetry, but as demonstrated in Fig. 4.2(D), this operation does not open up a band gap. Since shearing the bricklayer lattice does not open a gap, the Chern number calculation in Fig. 4.2(B) shows a white line at $\delta = 180^\circ$. We can conclude that broken time reversal symmetry is *not sufficient* to generate topology in gyroscopic metamaterials.

To study why breaking time reversal symmetry does not open a band-gap in this system we consider the weak-interaction limit, Eqn. 2.14.In this limit, we examine the net *chirality* of the canted bricklayer lattice by counting the total number of positive and negative phase loops in the unit cell [40].

Consider the movement of gyroscope n. The displacement of its neighbor, m, influences

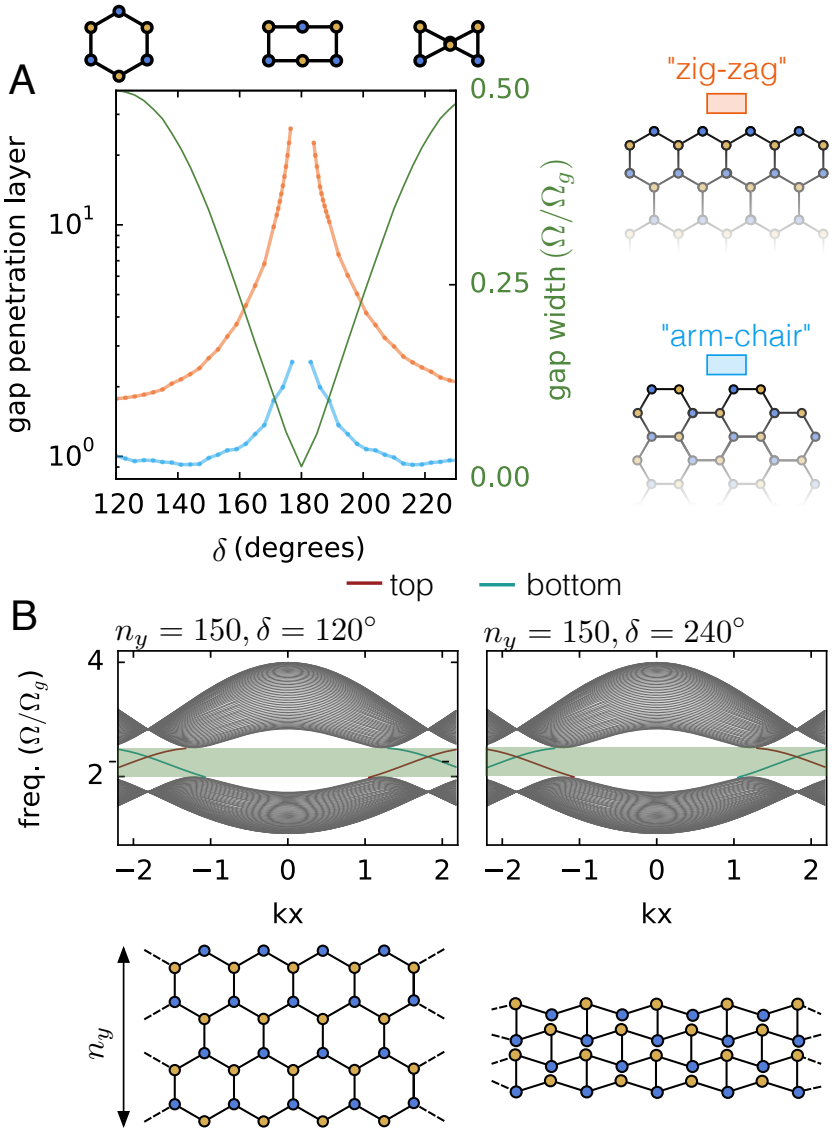

Figure 4.1: *Closing the gap, diverging length scales, and flipped edge modes (A)* The minimum penetration depth of the edge modes increases with decreasing gap with for both zig-zag (orange) and arm-chair (blue) edges in the honeycomb lattice. *(B)* The right-going excitations are on the top of the material when $\delta < 180°$ and switch for $\delta > 180°$.

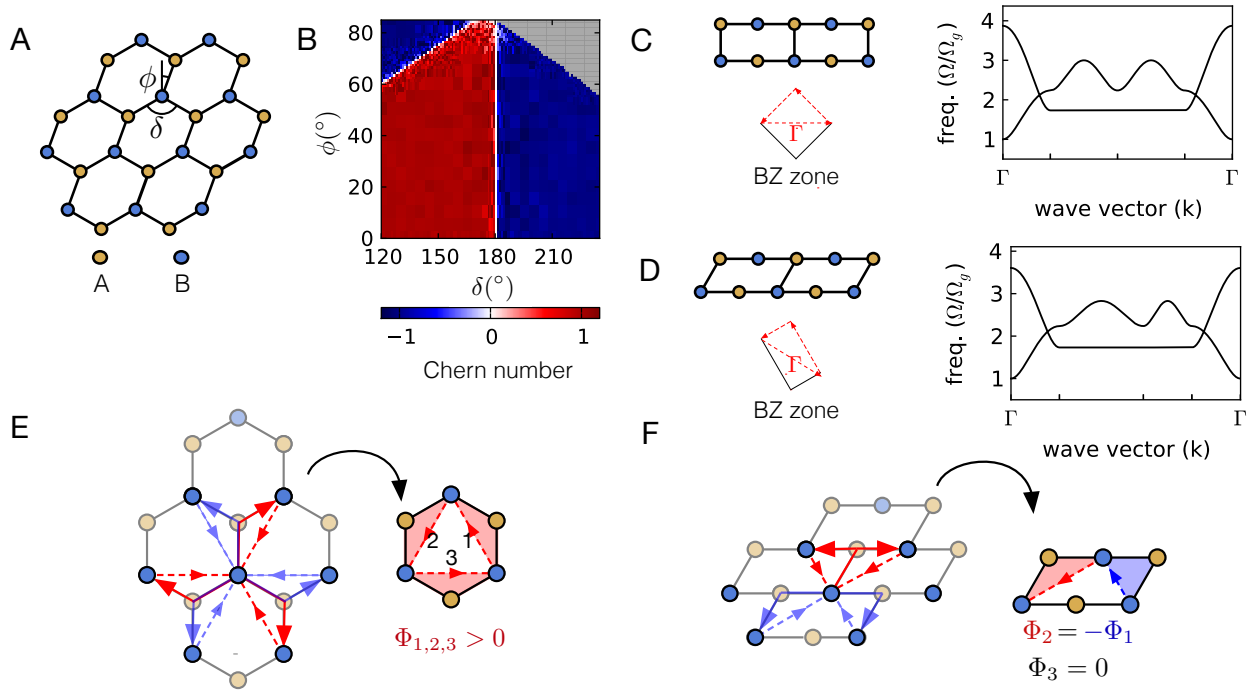

Figure 4.2: *Band-gaps and topology in the deformed honeycomb lattice. (A)* The angles ϕ and δ control the deformation of the honeycomb lattice. *(B)* The ϕ-δ phase diagram shows that the bulk Chern number the system changes when straight lines of bonds appear in the lattice. In this plot this occurs on the white diagonal line in the top left and on the white line in the center. *(C)* The band structure is plotted along paths in the Brillouin zone for examples where $\delta = 180°$. *C(top)* The gap is closed when $\phi = 0$. *C(bottom)* The band-gap does not open when $\phi \neq 0$, even though time reversal symmetry is broken. *D(left)* The phases introduced by coupling to the six next-nearest neighbors (shown in blue and red on the left) in a honeycomb lattice correspond to positive fluxes through areas enclosed by clockwise traversals of two nearest neighbor and one next-nearest neighbor. *D(right)* In the brick-layer lattice geometries there are two phases introduced by clockwise traversals of two nearest neighbor and one next-nearest neighbor. Because of this, the net chirality of this lattice is zero.

n's motion. The displacement of its next-nearest-neighbor (NNN), l, influences its motion as well, but only through the shared nearest neighbor, m. To leading order in the weakly interacting regime, the displacement of l that influences n appears shifted by a phase determined by the NNN bond angle, θ_{nml} (c.f. Eqn. 2.14). It is precisely these angles which determine the topological character of the band structure. In electronic tight-binding models, these six NNN couplings for each site correspond to phases introduced by traversing paths that enclose net magnetic flux.

We first calculate the phases, $2\theta_{nml}$, for the undeformed honeycomb lattice (Fig. 4.2 (E). There are three positive NNN hoppings (red arrows) and three negative ones (blue arrows) for each site, but this description is redundant: each set of three hoppings creates the same loop in a hexagonal plaquette, but with opposite chirality. Therefore, all six hoppings correspond to positive contributions for clockwise traversals of loops with two neighbors and one next-nearest neighbor, as shown in Fig. 4.2(E). This lattice has a net positive chirality as a consequence.

As we deform the honeycomb towards the brick-layer lattice, each configuration continues to have positive chirality in the same manner. The brick-layer unit cell, however, has two non-zero phase contributions which are equal in magnitude but opposite in sign, as shown in Fig. 4.2(F) right. This *continues* to remain true even if the brick-layer is sheared ($\phi \neq 0$). Because there is no net chirality in this deformation, no band-gap opens [40]. Even with other symmetries intact, breaking time reversal symmetry is an *insufficient* condition for a topological gyroscopic lattice.

In our explanation of the chirality demonstrated in Fig. 4.2E-F, we were able to predict whether or not edge states could be found. We additionally note that although we can gain insight into whether or not edge states can be found by studying the lattice bond angles, we cannot determine the *direction* of the edge states by studying the bond angles alone. Fig. 4.3A-B shows a lattice and band-structure that support both clockwise and counterclockwise propagating modes, Fig. 4.3C.

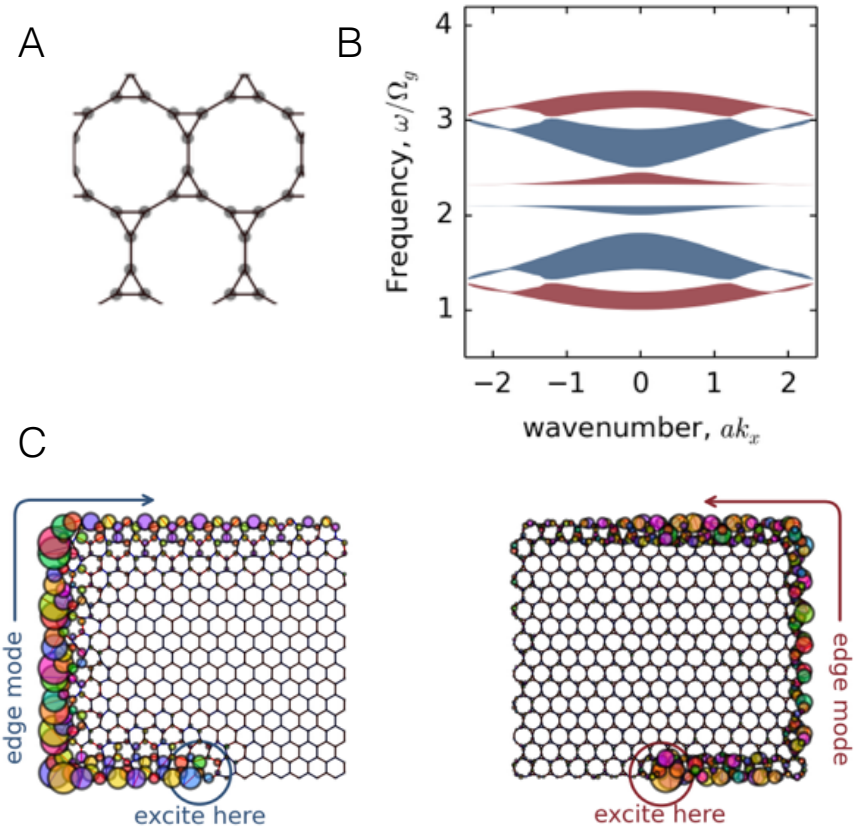

Figure 4.3: *Multi-direction edge excitations in one lattice. (A)* A lattice with six sites per unit cell, based on a honeycomb lattice construction. *(B)* The band-structure of the lattice shown in *(A)*. The lattice has 6 bands with two topological band gaps of opposite Chern number. *(C)* The gaps with opposite Chern numbers support edge states which propagate in opposite directions. Because the lattice can support both clockwise and counterclockwise excitations, we conclude that there is no intuitive way to find the direction of the edge state associated with a particular lattice.

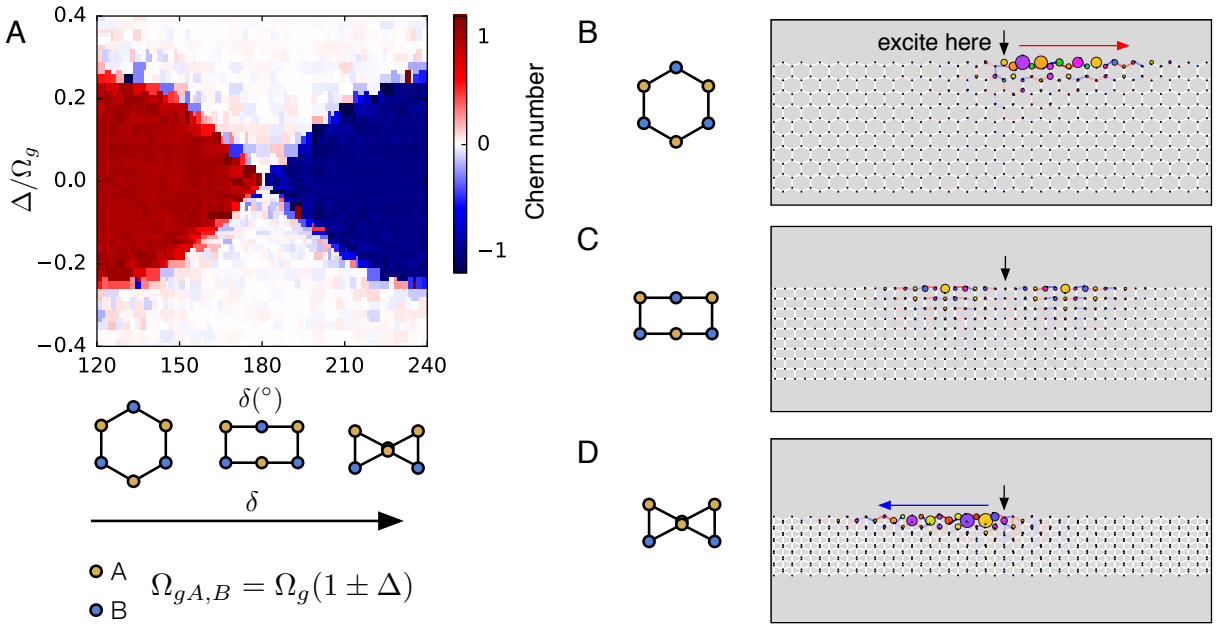

Figure 4.4: *Phase diagram for inversion and time reversal symmetries in a gyroscopic lattice.* The phase diagram for a deformed honeycomb lattice ($\phi = 0$) with varying Ω_g values on sites A and B is shown. Even when we are far from the Haldane model limit we find that the system shows the same interplay between two symmetries as the Haldane model prediction. In a simulation, gap excitaitons in Honeycomb*(B) (C)* When the geometry is a brick-layer the Chern number is 0 and unprotected modes propagate in both directions. *(D)* In the bowtie geometry propagate in opposite directions as predicted by a calculation of the Chern number.

4.3 Competing symmetries in topological gyroscopic systems

Our closest electronic counterpart, the Haldane model, displays an interplay between time reversal symmetry and inversion symmetry [2]. To study an analogous effect, we break the equivalence of the two interpenetrating triangular sublattices that comprise the honeycomb lattice by modulating their on-site gravitational precession frequencies : $\Omega_{gA,B} = \Omega_g(1 \pm \Delta)$.

Fig. 4.4(A) shows the phase diagram that results from varying δ and lattice pinning frequencies, $\Omega_{gA,B}$. When the unit cell's two sites are equivalent ($\Delta = 0$) the Chern number of the system changes only when the gap closes at the brick-layer transition. For $\Delta \neq 0$, however, a third, topologically trivial region appears. In this case, the band structure is gapped, yet displays no chiral edge modes. The behavior of excitations confirms the Chern

number calculations in all three regions, as indicated in Fig. 4.4(B-D) and **Movie S1**. In Fig. 4.4(C), excitations propagate along the edge in both directions. The Chern number is 0 and they are not topologically protected, and when disorder in motor spinning speeds is they begin to backscatter, **Movie S2**.

The result shown in Fig. 4.4(A) displays a strong resemblance to Haldane's phase diagram, where sites must be relatively equivalent to achieve topological states. However, we cannot conclude that balancing the gravitational precession frequencies on lattice sites will lead to topological excitations on all chiral gyroscopic lattices. Study of other lattices, see supplementary information for an example, with unequal coordination number show that site coordination also plays a role.

In fact, this conclusion needs a small correction. Some lattices have unequal coordination number of all the sites in the unit cell, see section 4.4 for more detail. When this is the case, we find through study of Eqn. 2.6, that the definition of equivalence includes coordination.

The first term in Eqn. 2.6 reveals that on-site pinning–where $\dot{\psi_p}$ depends on ψ_p–contributions come from the gravitational precession *as well as* from coupling to adjacent sites. Instead of balancing uncoupled on-site gravitational frequencies, we find that instead we must balance the following quantity,Ω_p, which we dub 'site pinning frequency,' for sites in a lattice:

$$\Omega_p = z\frac{\Omega_k}{2} + \Omega_g. \tag{4.1}$$

This result shows that site equivalence — just like time reversal — cannot be decoupled from the lattice.

4.4 Further discussion of topology in lattices

As stated above, gravitational precession frequency *and* coordination number contribute to on-site precession frequency for gyroscopes in a lattice. Here we demonstrate how unequal coordination number can affect lattice topology through study of an example lattice.

Fig. 4.5(A) shows an example of a lattice where sites in the unit cell have unequal coordination number. In this lattice, the A and B sites have coordination number of 4 while C and D have coordination number of 2.

When all gravitational precession frequencies are equal, top right corner of Fig. 4.5(B), the lattice displays no topological excitations. In accordance with eq:balance, the network becomes topological when Ω_{gA} and Ω_{gB} are reduced in comparison to Ω_{gC} and Ω_{gD}. As in Fig. 4.4, there is a neighborhood around balanced site pinning which allows for topological excitations.

So far, we've considered geometry deformations to the honeycomb lattice which allow for controlling the direction of excitation propagation. However, these deformations are not easily achievable because the honeycomb lattice is undercoordinated: a mechanical frame without fixed points would collapse with applied force. To create easily tunable metamaterials, however, our gyroscopes must sit on a lattice which can achieve uniform deformation with application of force at the material boundary. Here we explore the topology of the kagome lattice, which can be constructed such that the only non-localized zero energy mode is a uniformly collapsing mode [41]. As we will see, the lattice – which has three sites per unit cell – also has the property of having two topologically nontrivial band-gaps.

We note this lattice has been found to have interesting topological properties in other mechanical systems with time reversal symmetry. In mechanical systems, topological modes have been experimentally proposed and demonstrated for kagome and deformed kagome lattices with variation of lattice geometry [6, 17]. In these cases, variation of lattice geometry leads to a topological polarization which preferentially concentrates zero modes or states of self stress on one side of the material or at dislocations.

In order to investigate the topology of the kagome lattice under geometry deformations we employ the lattice distortion, shown in Fig. 4.6(A). Here the primitive vectors of the lattice are fixed as $a_{p+1} = (\cos(2\pi p/3), \sin(2\pi p/3))$. The positions of the lattice sites are described as $d_1 = a_1/2 + s_2$, $d_2 = a_2/2 - s_2$ and $d_3 = a_3/2$, where s_p describes the displacement of

d_{p-1} relative to the midpoint of the line along a_p. Following [6], these deformations can be represented by the independent variables x_1, x_2, x_3, and z so that $s_p = x_p(a_{p-1} - a_{p+1}) + \gamma_p a_p$ with $z = \gamma_1 + \gamma_2 + \gamma_3$.

The three bands and two band gaps in the vibrational spectrum of this lattice are shown in green in Fig. 4.6(B) for equivalent sites and geometry parameters $x_1 = 0, x_2 = x_3 = 0.1$. The Chern number of the lowest band is opposite that of the lowest band in the honeycomb lattice. The middle band has a Chern number of 0, and the top band has a Chern number opposite the bottom band.

Variation of lattice geometry has only a slight effect on the topology of the band structure, Fig. 4.6(C). In fact, for a lattice with equivalent lattice sites, the geometry variation has no effect on the system's topology. These results persist for variations of any single precession frequency and geometry parameter. Following Eqn. 1.1, we expect gap edge excitations to propagate counterclockwise around this material.

While lattice topology exhibits only a slight dependence on changes in a single lattice geometry parameter, the upper band gap can additionally be closed via simultaneous adjustment of all three lattice parameters. Tuning $x_1 = x_2 = x_3$ simultaneously yields the twisted kagome lattice. When the kagome lattice is in a pre-twisted state ($x_1 = x_2 = x_3 \neq 0$), a uniformly collapsing mode is admitted if a force is applied at the boundary, Fig. 4.7 (top) [41]. Using the parameterization above, the collapsed twisted kagome can be achieved by increasing the absolute value of x_1, x_2, x_3. However, this transformation does not preserve bond length and it is convenient instead to parameterize the degree of collapse using the bond twist angle as described in [6].

The width of the upper band gap may be controlled by adjustment of the degree of collapse of the lattice. As shown in Fig. 4.7, a slightly twisted lattice has the same three bands and two band-gaps as depicted in Fig. 4.6. However, the second band gap is closed as the degree of twist increases, Fig. 4.7 right. We therefore find that the topological properties of a twisted kagome metamaterial can be conveniently controlled by applying or releasing

stress on the boundary.

4.5 Conclusions

Our study of gyroscopic lattices has shown that a variety of different configurations ultimately result in topological edge states for gyroscopic materials. We have additionally learned that there are a few principles which govern topology in these systems, and now show how our findings can prove useful in the engineering of topological gyroscopic metamaterials.

From investigation of gyroscopic lattices, the principles can be summarized as follows:

I Breaking time reversal symmetry via bond angles is a necessary, but not sufficient condition for creating a lattice with a non-trivial band topology.

II A competition between time reversal symmetry and site equivalence determines whether or not a lattice can have topological modes. Lattice connectivity is relevant for determining the effective on-site precession frequencies to achieve equivalence.

A simple procedure, which essentially involves balancing site pinning frequencies according to lattice coordination and gravitational precession frequency as listed in Eqn. 4.1, can be employed to search for additional topological lattices.

The procedure allows us to generate lattices with desired properties—such as multiple band-gaps or mechanical stability—we show several examples in Fig. 4.8(A-D). A kagome-like lattice, shown in Fig. 4.8(A), has two topological band-gaps. As discussed in section 4.4, Kagome lattices are the simplest example of a two band-gap lattice, and promise applications for easily tunable control.

Fig. 4.8(B) shows a mechanically stable lattice. The coordination numbers for the sublattices are $z_A = z_C = 5$, and from our principles, we expect that $\Omega_B > \Omega_{A,C}$ for topological modes. Indeed, this principle holds true and nontrivial topology arises when the sites are relatively equivalent, Fig. 4.9.

Besides these two lattices, we find that even this simple procedure yields many other topological systems, two more of which are shown in Fig. 4.8(C-D). The results demonstrated in this work show that topology is not specific to one family of lattices in gyroscopic networks and in fact is quite general. Many topological lattices can be created using only simple principles–opening a myriad possibilities for material design.

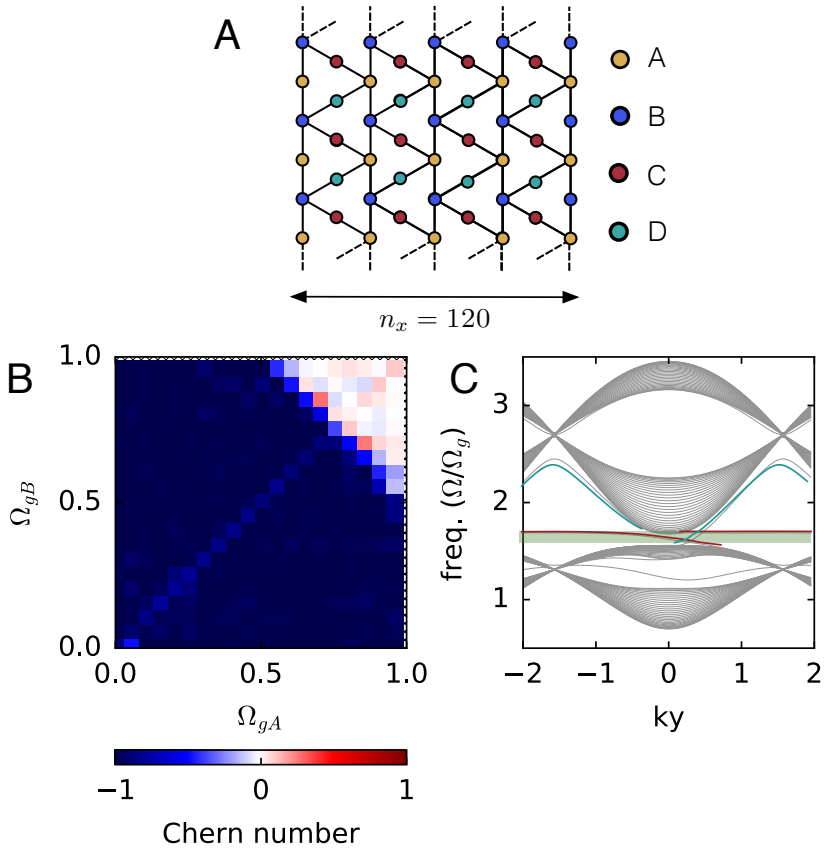

Figure 4.5: *Coordination number and topological phases.* Coordination number and topological phases. *(A)* A lattice with 4 lattice sites per unit cell, where sites A and B have a coordination number of 4 and sites C and D have a coordination number of 2. *(B)* The topological phase diagram for varying the gravitational precession frequencies on sites A and B. There are contributions to the on-site terms due to the lattice coordination. Because of the different coordination numbers for the lattice sites, the band structure is trivial when $\Omega_{gA} = \Omega_{gB} = \Omega_{gC} = \Omega_{gD}$. *(C)* The band structure for a strip which is infinite along y (shown in *(A)*).

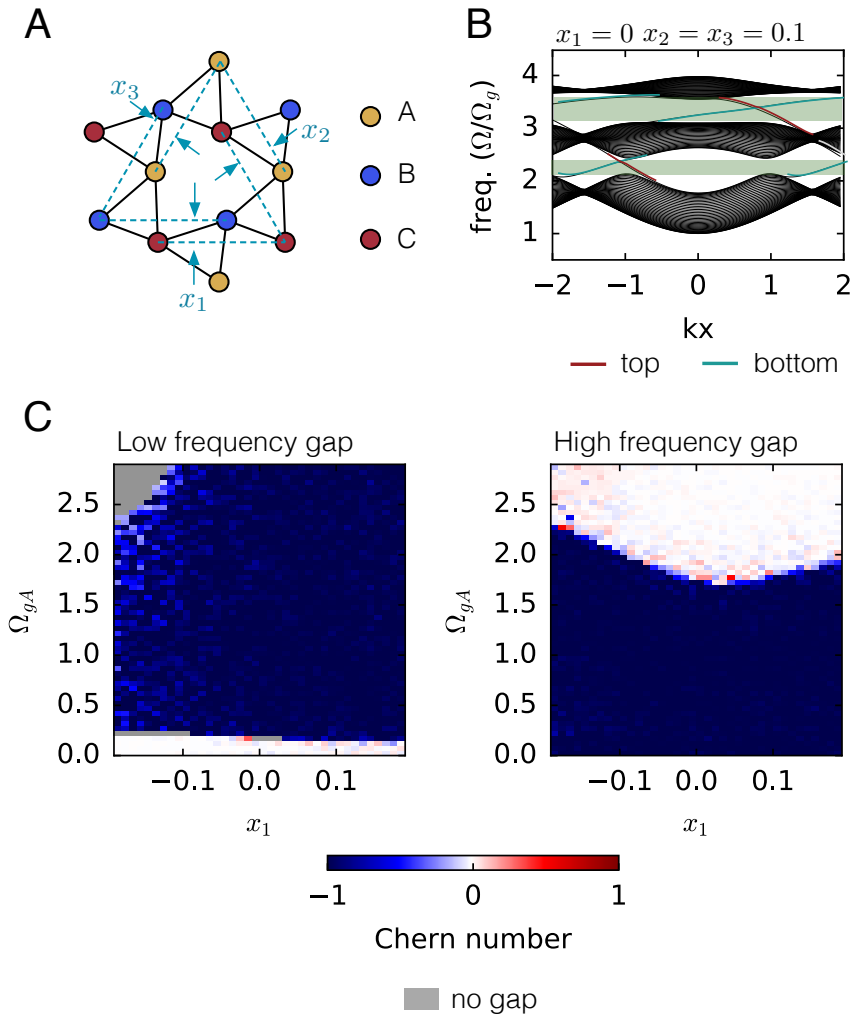

Figure 4.6: *Kagome lattice phase diagram and band structure.* Kagome lattice phase diagram and band structure *(A)* We consider deformations of the Kagome lattice using the parameterization given in [6] using geometry parameters x_1, x_2, x_3. *(B)* A calculation on a strip which is infinite along x (as depicted in A) shows that both gaps have edge modes which propagate in the same direction on the top edges. *(C)* The sum of band Chern numbers for bands below each gap is shown in the phase diagrams for each of the gaps. The Chern number has only a weak dependence on lattice geometry near the transition to a trivial topology in the second bandgap.

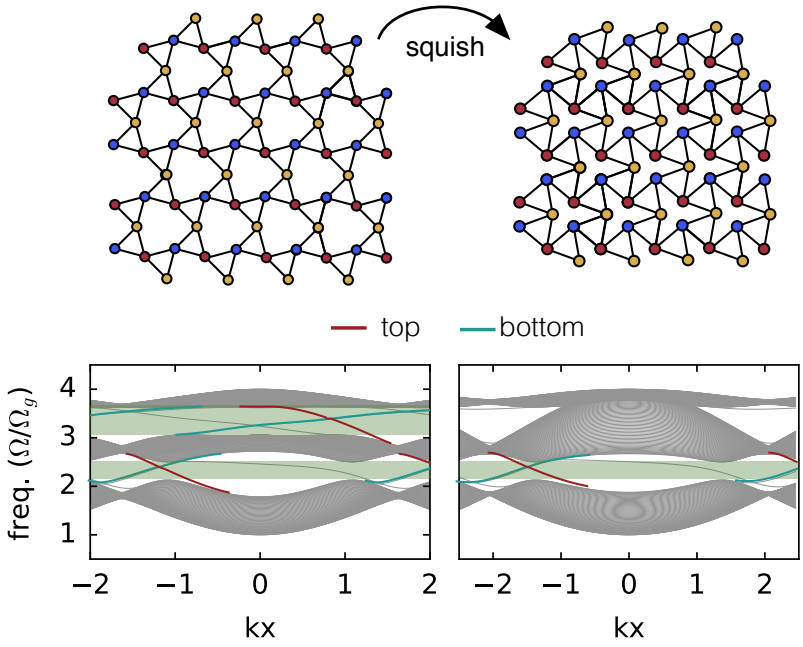

Figure 4.7: *Controlling the gap width in a gyroscopic metamaterial (A)* A twisted Kagome lattice can be squished on the edges to create a uniformly collapsing material. *(B)* The upper band gap closes when this operation is performed. This shows an example of an easily tunable band gap material.

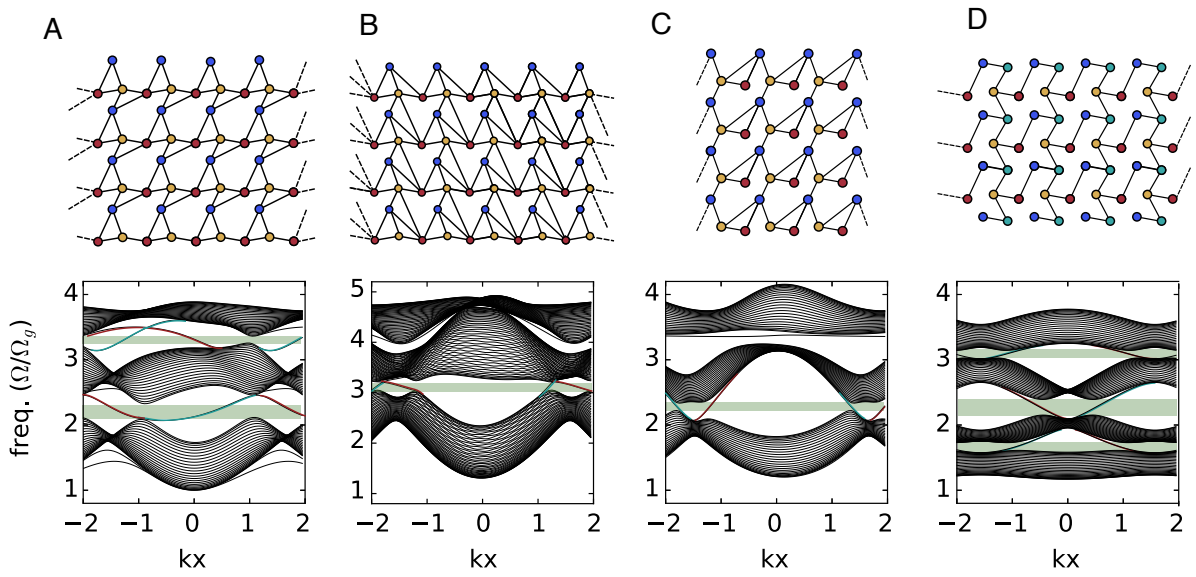

Figure 4.8: *Examples of topological lattices created with a simple procedure.* Lattices can be created with an algorithm in which points are placed in a square unit cell, repeated, and triangulated. Some bonds are deleted randomly. Examples of resulting band-structures are shown. *(A)*An example of a 3 site per unit cell lattice structure with two topological gaps. The propagation of edge modes is in the same direction as the kagome lattice. *(B)*A site per unit cell lattice structure with one topological gap (upper gap). The propagation of edge modes is in the same direction as the kagome lattice. *(C)*A 3 site per unit cell lattice structure with one topological gap (lowerr gap). The propagation of edge modes is in the same direction as the honeycomb lattice. *(D)*An example of a 4 site per unit cell lattice structure with three topological gaps. The propagation of edge modes is in the same direction as the kagome lattice for all three gaps.

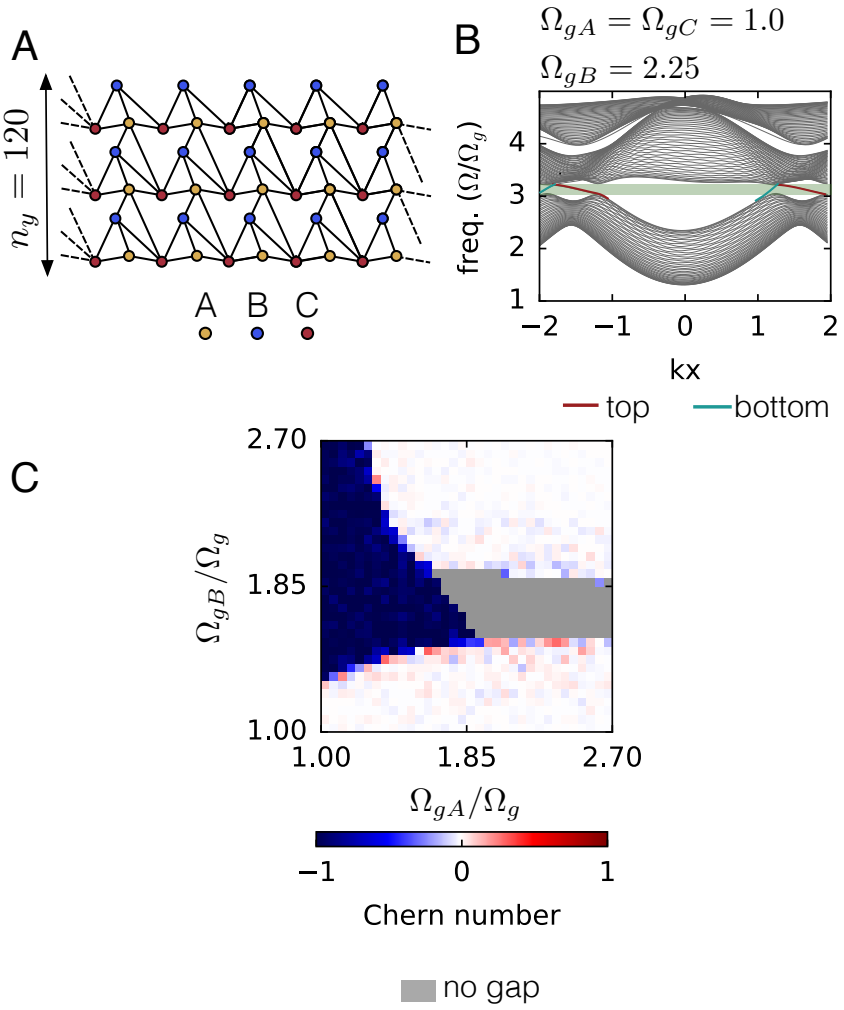

Figure 4.9: *Topology in a mechanically stable lattice. (A)* An semi-infinite strip of an example of a mechanically stable lattice with 3 sites in each unit cell. $z_A = 5$, $z_B = 4$, $z_C = 5$. *(B)* The band-structure of the semi-infinite strip shown in *(A)*

CHAPTER 5

TOPOLOGICAL PHASE TRANSITION IN EXPERIMENT

5.1 Introduction

Our gyroscopic materials fall into a larger set of mechanical metamaterials, which are artificial materials that derive their mechanical properties from their large scale structure rather than their composition. Often these materials are interesting from an applications standpoint because they can be engineered to have interesting properties such as negative Poisson ratio, tunable vibrational response, or vanishing shear modulus [42, 43]. Essential to the metamaterial usefulness, in many cases, is the ability to tune its mechanical properties.

An emerging class of mechanical metamaterials promise robust manipulation of mechanical modes bound to edges and dislocations. In particular, this thesis has discussed a metamaterial composed of gyroscopes on a lattice. In gyroscopic metamaterials, vibrational excitations, which are immune to backscattering and disorder, are able to propagate around edges despite irregularly shaped boundaries or other imperfections.

The ability to switch between halting and allowing these edge states would increase the functionality of these materials. Especially useful would be the ability to control edge state propagation in real time. In the case of our gyroscopic materials, our studies have shown that they are readily realized in an experimental system. Chapter 4 of this thesis theoretically demonstrated that a competition between inversion and time-reversal symmetries determines topology. Gyroscopic materials can become topologically trivial when inversion symmetry is broken strongly.

In this chapter, we combine these findings and explore the material property control by changing the competition between inversion and time-reversal symmetries in an experimental gyroscopic material. We show that tunable and reversible transitions between the topological and trivial phases can be achieved in experiment via modulation of the effective gravitational pinning frequencies on the two sublattices of the honeycomb lattice. This allows us to tune

our lattice from being topologically trivial to nontrivial in a reversible manner. Here, we show our preliminary results.

5.2 Experimental Topological Phase Transition on a Honeycomb Lattice

We now seek to observe the phase transition on the vertical axis of Fig. 4.4 in an experimental gyroscopic material. To induce this transition, we must vary the effective gravitational pinning strength on the A and B sublattices by shifting each by a value Δ, indicated in Fig. 5.1A. Conveniently, we may make use of our previous experimental set-up to cause the transition. As discussed in section 3.2, our experiment consists of 54 gyroscopes which are coupled to each other via a small magnet that is embedded in each spinning rotor. To vary sublattice pinning frequencies, we add a coil beneath each gyroscope as shown in Fig. 5.1B. By running varying current through the coils, we are able to control how tightly the gyroscopes are bound to their lattice positions.

For the phase transition experiments discussed in this chapter, the gyroscopes were additionally weighted down so that the base pinning frequency was equal to 1.5 Hz. We determined Δ values by measuring the precession frequencies of a single gyroscope over several coils. With tests of single gyroscopes above our coils, we find that we have control of the effective gravitational pinning frequencies over the range $\approx$ 0.9 - 2.1 Hz, as shown for one gyroscope in Fig. 5.1(C). To achieve pinning frequency modulation, we alternate the direction of the current in adjacent experimental coils.

We first examine the behavior of our lattice with a high Δ value($\approx$ 0.6 Hz). Unlike experiments with $\Delta = 0$ Fig. 5.2A, experiments with high Δ values do not support edge states that are able to propagate around the entire material boundary, Fig. 5.2B. At high Δ, we additionally observe that there seems to be a preferred direction for initial propagation direction that is set by motor spinning direction, see Fig. 5.2B, first panel, where the wave-

packet has high amplitude clockwise from the original excitation. When the motor spinning direction is reversed, we find that the wave packet direction is also initially reversed.

In order to ensure that this is not due to topology, we insert an obstacle in our material, Fig. 5.3A. Unlike topological states shown in Fig. 3.3B, now there is significant backscattering on this obstacle, indicating that the directional behavior is not due to topology in the materials' band structure. Our gyroscopic material is topologically trivial at high Δ values.

Having established that we may control the topology in our experiment, we next seek to induce a transition in order to arrest the propagation of an edge excitation. As shown in Fig. 5.3B, we find that the propagation of a wave packet in a topological gyroscopic material can be arrested by slowly increasing the current through the coils over the course of the experiment. Alternatively, we may decrease the current through the coils to allow edge state propagation – the transition is completely reversible in our metamaterial.

The experiments presented in this chapter provide a proof of concept for inducing a phase transition in a gyroscopic lattice. We note, however, that there is a large uncertainty range on the transition value Δ because of experimental variation in coil field strength. Fig. 5.1(C) shows the variation in Δ strength for a single gyroscope tested on several single coils in the experiment. The variation, of around is likely due to variation in height of gyroscopes over coils. The disorder in Δ values may complicate measurement of the transition value. An avenue of future work is exploring this transition in more depth by increasing the precision of Δ values.

5.3 Conclusions

We have demonstrated that topological transitions are realizable in experimental gyroscopic materials via modulation of on-site pinning frequencies in the lattice. This demonstration paves the way for controllable topological materials, where edge mode propagation can be initiated and halted on demand. The preliminary results presented in this chapter is the first step towards tunable gyroscopic materials. Combined with findings in section 4.4, these

results indicate that metamaterials constructed from gyroscopes can be incredibly versatile: band-gaps can be closed or rendered topologically trivial with simple methods.

Besides the ability to tune mechanical properties, this experimental system also provides future opportunities to measure scaling relationships near the topological phase transition and directly measure Berry curvature via the deviation of wave-packets in trivial and non-trivial states. Future work with this experiment include improving the system disorder via controlling the motor spinning speeds more directly and reducing the uncertainty in the change in pinning frequency caused by each coil.

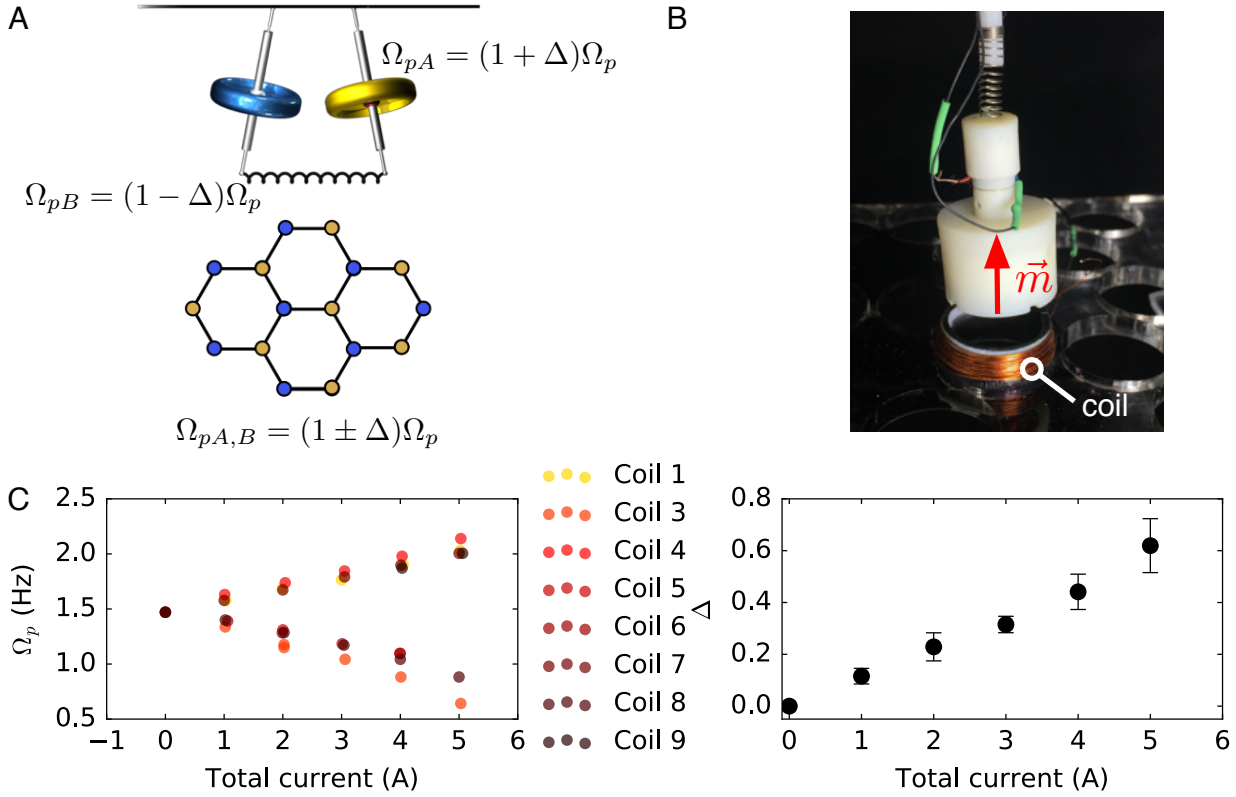

Figure 5.1: *Experimental set-up to induce a phase transition in a lattice. (A)* The phase transition we are studying requires modulating the pinning frequencies, or effective gravitational pinning frequencies, on the A and B sublattices. We shift sublattice A up by Δ and sublattice B down by Δ. *(B)* This can be achieved experimentally by coupling the magnet in each gyroscope to a coil that sits beneath it. The magnetic field can pull the gyroscope down or push it up, depending on the direction of current through the coil. *(C) Left* Ω_p values for a single gyroscope over several coils in the experiment as the current is varied. Each coil has 1/5 of the total current through it. There is a noticeable spread in Ω_p values for a particular current. *(C) Right* Δ values from data on the left. The error bars are plotted as the standard deviation of the data to portray of the spread/variation in Δ values in the experiment.

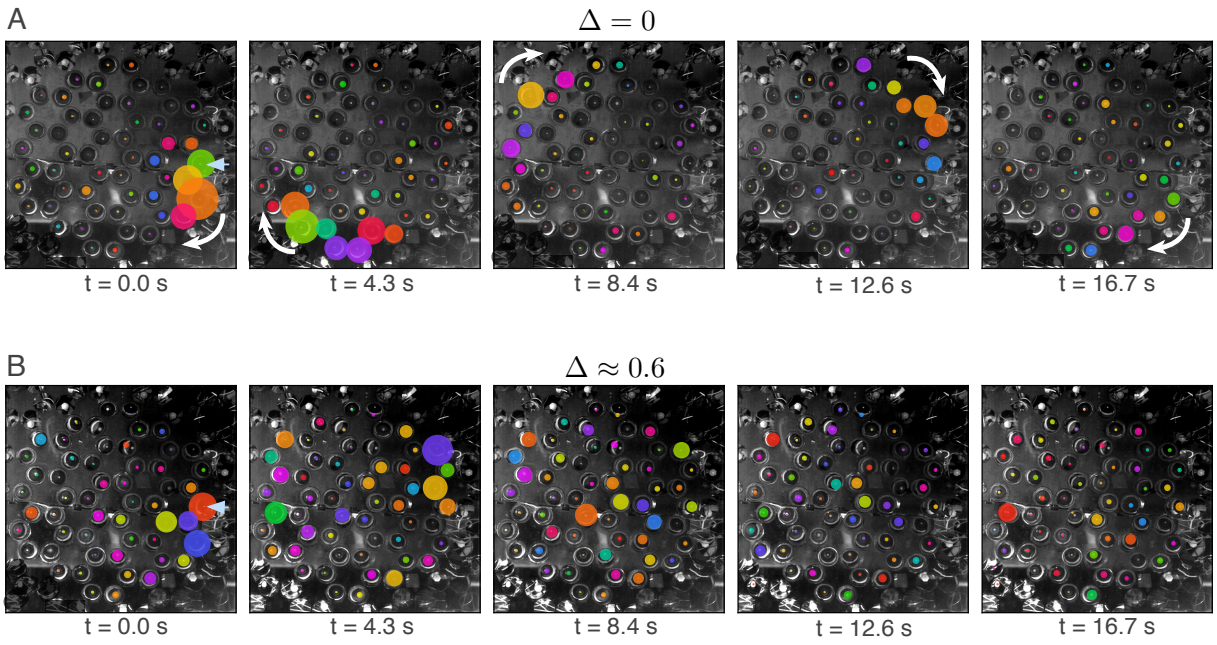

Figure 5.2: *Comparision between* $\Delta = 0$ *and* $\Delta \approx 0.6$ *in experiment. (A)* When $\Delta = 0$ a gap-frequency excitation propagates around the edge of the material–making one full transversal. *(B)*When we increase Δ in the experiment, we no longer observe unidirectional edge mode propagation, though there does seem to be a bias in the initial propagation direction of the excitation.

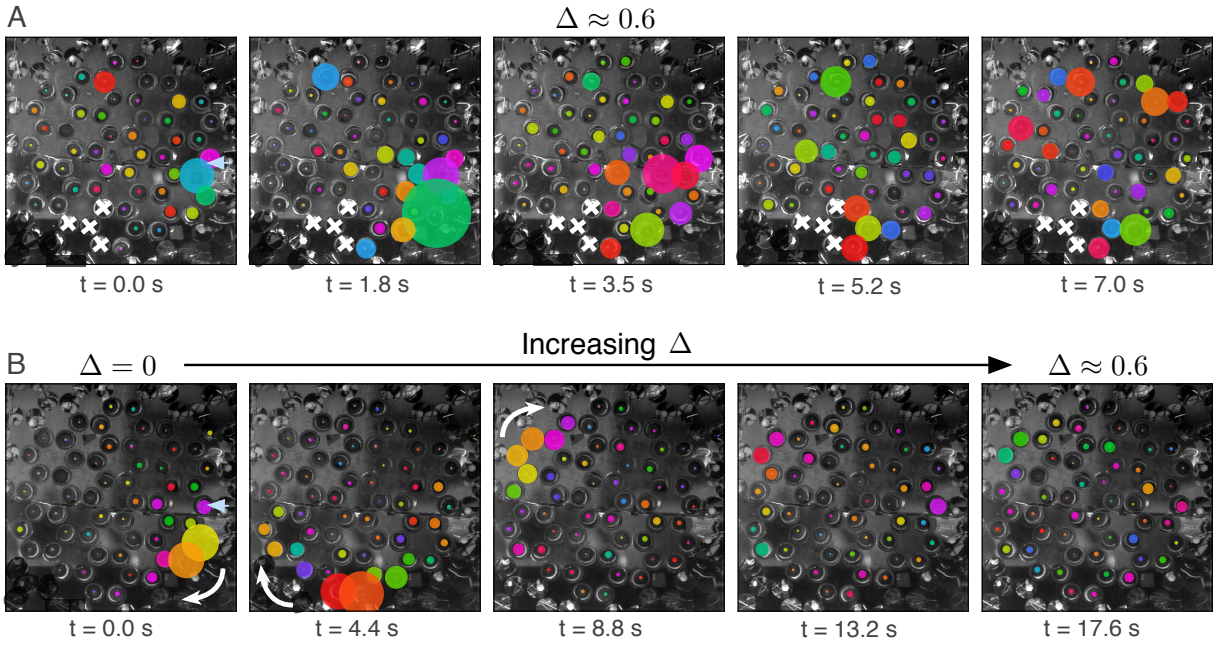

Figure 5.3: *Obstacle at high* Δ *and arresting excitation propagation by changing* Δ. *(A)* When $\Delta \approx 0.6$ excitations that were in the gap at $\Delta = 0$ seem to have a directional bias in their initial propagation direction. However, they scatter easily off obstacles. The white X marks indicate where gyroscopes have been removed and replaced by magnets. *(B)*A propagating edge state stopped by increasing the value of Δ over the course of the experiment. Here an excitation initially propagated clockwise, but stopped due to the high Δ value by the fourth frame from the left.

CHAPTER 6

EXTENSION TO AMORPHOUS MATERIALS

6.1 Introduction

Thus far this thesis has considered gyroscopes in systems with underlying spatial order through study of lattices. However, it is likely that avenues of creating topological gyroscopic metamaterials, such as self-assembly, may be imperfect and lack global spatial order.

Historically, ordered systems have been the focus of study in condensed matter physics because their behavior can be easily captured and analyzed with momentum-space descriptions. Understanding amorphous materials, on the other hand, has proved to be more challenging [44]. Particularly important for applications of gyroscopic metamaterials is understanding concepts of bandgaps and topological behavior. Even in the electronic setting these properties are not well understood for amorphous materials.

We have shown that our gyroscopic material's topological properties are robust against the addition of what is known as"δ-correlated" disorder, which was introduced due to spread in motor spinning speed. However, this robustness against δ-correlated disorder does not necessarily imply that that the edge states should be immune to disorder that disrupts their spatial order. This is because topological insulator states require the existence of delocalized states in each nontrivial band, unlike conventional insulators whose electronic states can be thought of as a sum of independent local insulating states [45, 46, 47].

The extent to which spatial order needs to be built into the structure that gives rise to topological modes is unclear. This chapter contains a recipe for constructing amorphous arrangements of interacting gyroscopes—structurally more akin to a liquid than a solid—that naturally support topological phonon spectra. Once again, we find that topology in these systems can be characterized by a Chern number. For amorphous systems we turn to a method of calculation by Kitaev, which had been previously developed for electronic lattice systems with disorder in on-site energies [48].

We find that we can tune the chirality of edge modes to be either clockwise or counter-clockwise by creating amorphous structures which are locally akin to their lattice counterparts. Our results show that topology, a nonlocal property, can naturally arise in materials for which the only design principle is the local connectivity. Such a design principle lends itself to imperfect manufacturing and self-assembly.

6.2 Creation of Amorphous Networks

Essential to the existence of topological edge states in gyroscopic metamaterials is the existence of a band-gap. Random hyperuniform or jammed triangulated point-sets, unfortunately lack this quality and were not found to be amenable to the study of topology in gyroscopic systems.

In order to create a system with a band-gap, we turned to a construction that is a Voronoi tessellation with either Wigner-Seitz construction or by connecting centroids of a triangulation [49]. In this construction, we place gyroscopes at the edges of the tessellation verticies and find a network that is locally akin to a honeycomb lattice, Fig. 6.1(A). We find that the placement of the band-gap is determined by the gravitational pinning strength and pinning interaction strength, and that it overlaps directly with the band-gap in the corresponding honeycomb lattice system.

Crucially, we find that our structures show hallmarks of non-trivial topology. When the system is cut to a finite size, modes confined to the edge populate the mobility gap, mixed in with localized states. As shown in the direct simulations of Fig. 6.1(B), shaking a gyroscope on the boundary results in chiral waves that are both robust against disorder and immune to backscattering.

We constructed an experimental realization using our magnetically interacting gyroscopes, as shown in Figure 6.1C. Our experiment is a realization of 195 gyroscopes in a Voronized network based on a jammed point set. Once again, the band structure's topology is not affected by the substantial differences between long-range magnetic interaction

and linear springs. As in previous experiments, these gyroscopes are constructed from 3D-printed units encasing DC motors which interact via magnetic repulsion. However, we note that variations in bond lengths and motor spinning speeds (each of $\sim 10\%$) additionally introduce substantial disorder in the system. Probing the edge of this system immediately generates a chiral wave packet localized to the boundary, confirming that this class of topological material is physically realizable and robust (Fig. 6.1C) against spatial variation and strong δ-correlated disorder. Real-space calculations of the Chern number using the Kitaev method confirm the topology of our network.

Using the insight that our network looks locally similar to a honeycomb lattice, we use our findings on the kagome lattice in chapter 4 to create a network with opposite Chern number. When the construction shown in Fig. 6.2 is performed, we find the presence of topologically protected modes with opposite direction and the corresponding opposite Chern number in the the band structure. The band-gaps in lattices that are locally akin to kagome lattices overlap with the bandgaps in the kagome lattice. It seems that amorphous networks which are locally akin to lattices are topologically similar to their lattice counterparts.

6.3 Conclusions

The results presented here have demonstrated that topology is achievable without global spatial order in gyroscopic metamaterials. Voronoized networks, which are locally akin to a honeycomb lattice, have the same topological classification as honeycomb lattices. An alternate decoration based on the kagome lattice, displays the same topology and edge state propagation direction as the kagome lattice.

Our study demonstrates that local interactions and local geometric arrangement are sufficient to generate chiral edge modes on the scale of the system size, promising new avenues the engineering of topological mechanical metamaterials generated via imperfect self-assembly processes.

Real space Chern number calculation methods, like Kitaev's, also open avenues for direct

measurement of Chern numbers in experimental systems. This has not yet been attempted in gyroscopic metamaterials, but could be explored in future projects.

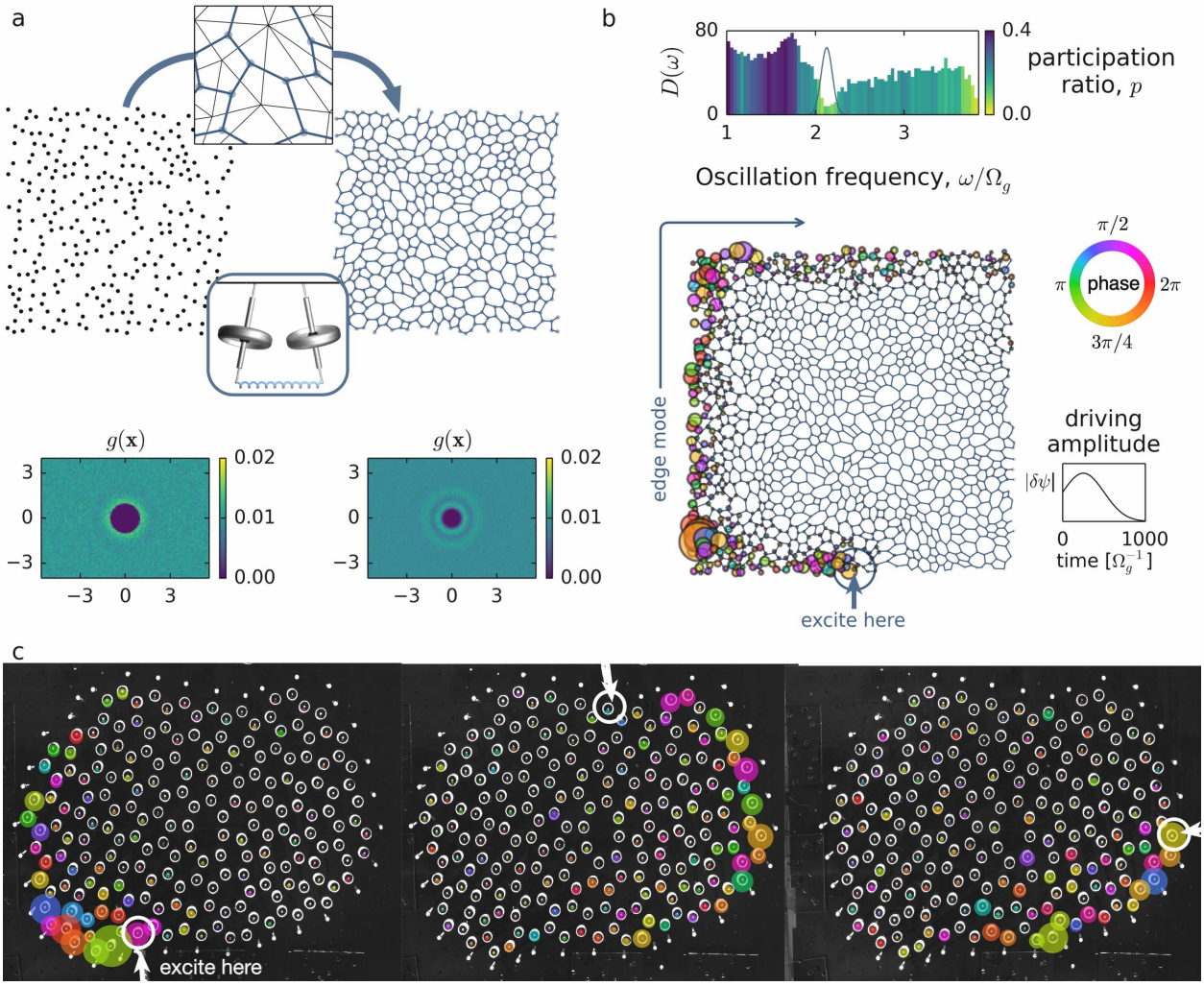

Figure 6.1: *Local structure gives rise to chiral edge modes (A)* Voronoization of an amorphous structure, constructed by connecting adjacent centroids of a triangulation, preserves isotropy and lack of long-range order, here with a hyperuniform point set. Two-point correlation functions (below) are shown for a system of $N \approx 3000$ particles. *(B)* Simulations reveal chiral edge modes in topological gyroscopic networks. The localization of modes is probed by participation ratio, $p = \left(\sum_i |\psi_i|^2\right)^2 / N \sum_i |\psi_i|^4$, and the density of states is plotted as a function of normal mode oscillation frequency, in units of the gravitational precession frequency, $\Omega_g = lmg/I\omega$. The blue curve overlaying over the density of states denotes the frequency of the driving excitation in the simulation. Here, the characteristic spring frequency, $\Omega_k = kl^2/I\omega$ is chosen such that $\Omega_g = \Omega_k$. The inset on the right shows the amplitude, $|\delta\psi|$, of the displacement for the single gyroscope which is shaken at a constant frequency. *C* Edge mode propagating in an amorphous experimental gyroscopic network. The motor- driven gyroscopes couple via a magnetic dipole-dipole interaction. Despite the nonlinear interaction and spinning speed disorder ($\sim$ 10%), the edge mode appears, no matter where the excitation is initialized.

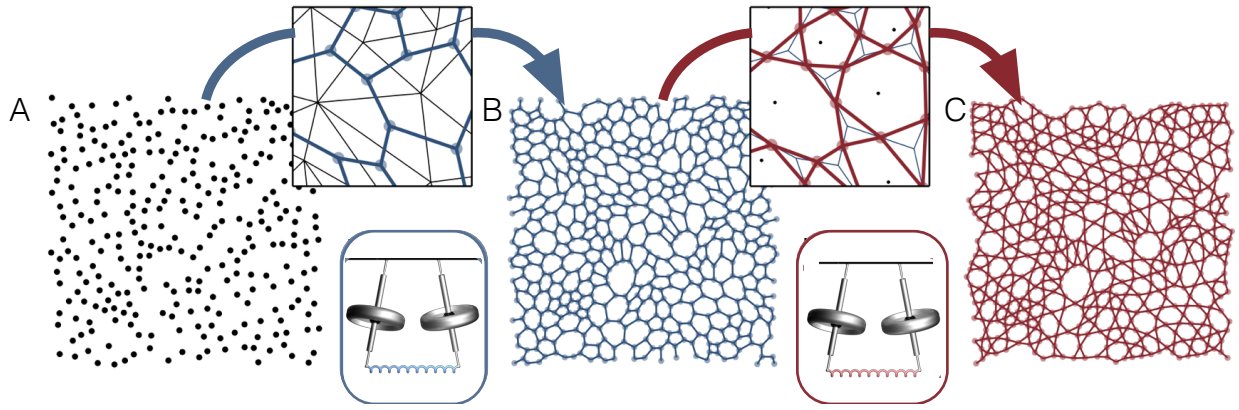

Figure 6.2: *Amorphous network construction for Voronized and Kagomized Point-Sets* *(A)* We begin with a random point-set. Although jammed or hyperuniform configurations can be used, the specifics of the random point-set creation do not seem to be important in system topology. *(B)* Our first construction is a voronization. It is constructed by connecting adjacent centriods of a triangulation. *(C)* A second decoration can be used to engineer systems which have oppositely propagating edge states. In the kagomazation construction, gyroscopes are placed at the midpoint of each of the voronized edges and connected to gyroscopes on the adjacent edges. Like the kagome lattice, edge states in the amorphous kagome propagate counter-clockwise.

CHAPTER 7

CONCLUSION AND OUTLOOK

This thesis has presented an experimental and theoretical exploration of topological gyroscopic metamaterials. Our theoretical work has shown that nontrivial band topology is easily achievable in gyrosopic systems. The details of lattice structure do not significantly affect topology, and we have uncovered a simple prescription for creation of topological lattices. We found that edge state direction cannot be predicted using simple methods and showed that there are lattices which have edge states that propagate in both directions. Building on our lattice observations, we have additionally shown that topological edge states can be achieved even in materials without underlying spatial order by studying amorphous systems. We found that the topological properties are insensitive to the underlying pointset and are instead determined by which lattice the network locally resembles.

Our direct experimental observations have demonstrated that the edge states in a gyroscopic metamaterial are incredibly robust. We have observed edge mode propagation in nontrivial lattices and amorphous networks. We have additionally shown that gyroscopic metamaterials can be tunable by inducing a phase transition in a real material. Our results show that gyroscopic band topology can be easily manipulated, and pave the way for gyroscopic material control.

Future directions of study could include investigating the behavior of gyroscopic systems in the nonlinear regime. Other work, has shown that nonlinearities can lead to interesting properties in other topological systems [7, 50, 51]. Also of interest are measurements of Berry curvature or direct measurements of the Chern number in experimental systems. These measurements may become feasible as the experimental system is improved and the spread in motor spinning speed is narrowed.

Other avenues of study could include scaling down the gyroscopic materials. The current experiment is macroscopically sized and each gyroscope must be constructed by hand. Any practical application would need scaled down size, and scaled up production capabilities.

The work presented here has elucidated principles behind topological gyroscopic material properties and design. Though much has been uncovered, there are still open questions and interesting physics to pursue in these systems.

REFERENCES

[1] C. L. Kane and E. J. Mele. Quantum Spin Hall Effect in Graphene. *Physical Review Letters*, 95(22):226801, November 2005.

[2] F.D.M. Haldane. Model for a Quantum Hall Effect without Landau Levels: Condensed-Matter Realization of the "Parity Anomaly". *Physical Review Letters*, 61(18):2015–2018, October 1988.

[3] M. Z. Hasan and C. L. Kane. Colloquium : Topological insulators. *Reviews of Modern Physics*, 82(4):3045–3067, November 2010.

[4] F. D. M. Haldane and S. Raghu. Possible Realization of Directional Optical Waveguides in Photonic Crystals with Broken Time-Reversal Symmetry. *Physical Review Letters*, 100(1):013904, January 2008.

[5] Emil Prodan and Camelia Prodan. Topological Phonon Modes and Their Role in Dynamic Instability of Microtubules. *Physical Review Letters*, 103(24):248101, December 2009.

[6] C. L. Kane and T. C. Lubensky. Topological boundary modes in isostatic lattices. *Nature Physics*, 10(1):39–45, December 2013.

[7] Bryan Gin-ge Chen, Nitin Upadhyaya, and Vincenzo Vitelli. Nonlinear conduction via solitons in a topological mechanical insulator. *Proceedings of the National Academy of Sciences*, 111(36):13004–13009, September 2014.

[8] Roman Süsstrunk and Sebastian D. Huber. Classification of topological phonons in linear mechanical metamaterials. *Proceedings of the National Academy of Sciences*, 113(33):E4767–E4775, August 2016.

[9] J. E. Avron, R. Seiler, and B. Simon. Homotopy and Quantization in Condensed Matter Physics. *Physical Review Letters*, 51(1):51–53, July 1983.

[10] Gregor Jotzu, Michael Messer, Remi Desbuquois, Martin Lebrat, Thomas Uehlinger, Daniel Greif, and Tilman Esslinger. Experimental realization of the topological Haldane model with ultracold fermions. *Nature*, 515(7526):237–240, November 2014.

[11] J. Clerk Maxwell. On the calculation of the equilibrium and stiffness of frames. *The London, Edinburgh, and Dublin Philosophical Magazine and Journal of Science*, 27(182):294–299, 1864.

[12] Z. Y. Wei, Z. V. Guo, L. Dudte, H. Y. Liang, and L. Mahadevan. Geometric Mechanics of Periodic Pleated Origami. *Physical Review Letters*, 110(21):215501, May 2013.

[13] M. F. Thorpe. Continuous deformations in random networks. *J Non Cryst Solids*, 57(3):355–370, September 1983.

[14] M Wyart, S. R Nagel, and T. A Witten. Geometric origin of excess low-frequency vibrational modes in weakly connected amorphous solids. *Europhysics Letters*, 72(3):486–492, November 2005.

[15] T C Lubensky, C L Kane, Xiaoming Mao, A Souslov, and Kai Sun. Phonons and elasticity in critically coordinated lattices. *Reports on Progress in Physics*, 78(7):073901, July 2015.

[16] Sung Hoon Kang, Sicong Shan, Andrej Košmrlj, Wim L. Noorduin, Samuel Shian, James C. Weaver, David R. Clarke, and Katia Bertoldi. Complex Ordered Patterns in Mechanical Instability Induced Geometrically Frustrated Triangular Cellular Structures. *Physical Review Letters*, 112(9):098701, March 2014.

[17] Jayson Paulose, Bryan Gin-ge Chen, and Vincenzo Vitelli. Topological modes bound to dislocations in mechanical metamaterials. *Nature Physics*, 11(2):153–156, January 2015.

[18] Vincenzo Vitelli, Nitin Upadhyaya, and Bryan Gin-ge Chen. Topological mechanisms as classical spinor fields. *arXiv:1407.2890 [cond-mat, physics:hep-th]*, July 2014.

[19] Zheng Wang, Yidong Chong, J. D. Joannopoulos, and Marin Soljacic. Observation of unidirectional backscattering-immune topological electromagnetic states. *Nature*, 461(7265):772–775, October 2009.

[20] Nina Berg, Kira Joel, Miriam Koolyk, and Emil Prodan. Topological phonon modes in filamentary structures. *Physical Review E*, 83(2):021913, February 2011.

[21] Zhaoju Yang, Fei Gao, Xihang Shi, Xiao Lin, Zhen Gao, Yidong Chong, and Baile Zhang. Topological Acoustics. *Physical Review Letters*, 114(11):114301, March 2015.

[22] Hafezi, M., Mittal, S., Fan, J., Migdall, A., and Taylor, J. M. Imaging topological edge states in silicon photonics. *Nature Photonics*, 7(12):1001–1005, December 2013.

[23] Mikael C. Rechtsman, Julia M. Zeuner, Yonatan Plotnik, Yaakov Lumer, Daniel Podolsky, Felix Dreisow, Stefan Nolte, Mordechai Segev, and Alexander Szameit. Photonic Floquet topological insulators. *Nature*, 496(7444):196–200, April 2013.

[24] Roman Süsstrunk and Sebastian D. Huber. Observation of phononic helical edge states in a mechanical topological insulator. *Science*, 349(6243):47–50, July 2015.

[25] V. Peano, C. Brendel, M. Schmidt, and F. Marquardt. Topological Phases of Sound and Light. *Physical Review X*, 5(3):031011, July 2015.

[26] Jia Ningyuan, Clai Owens, Ariel Sommer, David Schuster, and Jonathan Simon. Time- and Site-Resolved Dynamics in a Topological Circuit. *Physical Review X*, 5(2):021031, June 2015.

[27] S. Raghu and F. Haldane. Analogs of quantum-Hall-effect edge states in photonic crystals. *Physical Review A*, 78(3):033834, September 2008.

[28] Zheng Wang, Y. D. Chong, John D. Joannopoulos, and Marin Soljačić. Reflection-Free One-Way Edge Modes in a Gyromagnetic Photonic Crystal. *Physical Review Letters*, 100(1):013905, January 2008.

[29] A. A. Maradudin. Some effects of point defects on the vibrations of crystal lattices. *Reports on Progress in Physics*, 28(1):331–380, 1965.

[30] D. J. Thouless, M. Kohmoto, M. P. Nightingale, and M. den Nijs. Quantized Hall Conductance in a Two-Dimensional Periodic Potential. *Physical Review Letters*, 49(6):405–408, August 1982.

[31] Meng Xiao, Guancong Ma, Zhiyu Yang, Ping Sheng, Z. Q. Zhang, and C. T. Chan. Geometric phase and band inversion in periodic acoustic systems. *Nature Physics*, 11(3):240–244, March 2015.

[32] J. Prost, F. Jülicher, and J-F. Joanny. Active gel physics. *Nature Physics*, 11(2):111–117, February 2015.

[33] Jeremie Palacci, Stefano Sacanna, Asher Preska Steinberg, David J. Pine, and Paul M. Chaikin. Living Crystals of Light-Activated Colloidal Surfers. *Science*, 339(6122):936–940, February 2013.

[34] K. v Klitzing, Gerhard Dorda, and Michael Pepper. New method for high-accuracy determination of the fine-structure constant based on quantized Hall resistance. *Physical Review Letters*, 45(6):494, 1980.

[35] Pai Wang, Ling Lu, and Katia Bertoldi. Topological Phononic Crystals with One-Way Elastic Edge Waves. *Physical Review Letters*, 115(10), September 2015.

[36] B. G. Chen, N. Upadhyaya, and V. Vitelli. Nonlinear conduction via solitons in a topological mechanical insulator. *Proceedings of the National Academy of Sciences*, 111(36):13004–13009, September 2014.

[37] Lisa M. Nash, Dustin Kleckner, Alismari Read, Vincenzo Vitelli, Ari M. Turner, and William T. M. Irvine. Topological mechanics of gyroscopic metamaterials. *Proceedings of the National Academy of Sciences*, 112(47):14495–14500, November 2015.

[38] Romain Fleury, Alexander B Khanikaev, and Andrea Alù. Floquet topological insulators for sound. *Nature Communications*, 7:11744, June 2016.

[39] Yao-Ting Wang, Pi-Gang Luan, and Shuang Zhang. Coriolis force induced topological order for classical mechanical vibrations. *New Journal of Physics*, 17(7):073031, July 2015.

[40] Anthony R. Wright. Realising Haldane's vision for a Chern insulator in buckled lattices. *Scientific Reports*, 3, September 2013.

[41] Gaoxiang Wu, Yigil Cho, In-Suk Choi, Dengteng Ge, Ju Li, Heung Nam Han, Tom Lubensky, and Shu Yang. Directing the Deformation Paths of Soft Metamaterials with Prescribed Asymmetric Units. *Advanced Materials*, 27(17):2747–2752, May 2015.

[42] Bastiaan Florijn, Corentin Coulais, and Martin van Hecke. Programmable Mechanical Metamaterials. *Physical Review Letters*, 113(17), October 2014.

[43] Stephan Ulrich, Nitin Upadhyaya, Bas van Opheusden, and Vincenzo Vitelli. Shear shocks in fragile networks. *Proceedings of the National Academy of Sciences*, 110(52):20929–20934, December 2013.

[44] P. M. Chaikin and T. C. Lubensky. *Principles of Condensed Matter Physics*. Cambridge University Press, September 2000. Google-Books-ID: P9YjNjzr9OIC.

[45] D. J. Thouless. Wannier functions for magnetic sub-bands. *Journal of Physics C: Solid State Physics*, 17(12):L325, 1984.

[46] Y. Huo and R. N. Bhatt. Current carrying states in the lowest Landau level. *Physical Review Letters*, 68(9):1375–1378, March 1992.

[47] T. Thonhauser and David Vanderbilt. Insulator/Chern-insulator transition in the Haldane model. *Physical Review B*, 74(23):235111, December 2006.

[48] Alexei Kitaev. Anyons in an exactly solved model and beyond. *Annals of Physics*, 321(1):2–111, January 2006.

[49] Marian Florescu, Salvatore Torquato, and Paul J. Steinhardt. Designer disordered materials with large, complete photonic band gaps. *Proceedings of the National Academy of Sciences*, 106(49):20658–20663, August 2009.

[50] Yaakov Lumer, Yonatan Plotnik, Mikael C. Rechtsman, and Mordechai Segev. Self-Localized States in Photonic Topological Insulators. *Physical Review Letters*, 111(24):243905, December 2013.

[51] Yaakov Lumer, Mikael C. Rechtsman, Yonatan Plotnik, and Mordechai Segev. Instability of bosonic topological edge states in the presence of interactions. *Physical Review A*, 94(2):021801, August 2016.